International Journal of Multiphase Flow 37 (2011) 1072–1092

Contents lists available at ScienceDirect

International Journal of Multiphase Flow

journal homepage: www.elsevier.com/locate/ijmulflow

Drag law for monodisperse gas–solid systems using particle-resolved direct numerical simulation of flow past fixed assemblies of spheres

S. Tenneti, R. Garg, S. Subramaniam *

Department of Mechanical Engineering, Center for Computational Thermal-fluids Research, Iowa State University, Ames, IA 50011, USA

ARTICLE INFO

Article history:
Received 5 February 2011
Received in revised form 12 May 2011
Accepted 17 May 2011
Available online 25 May 2011

Keywords:
Drag law
Gas–solid flow
Particle-resolved direct numerical simulation
Immersed boundary method

ABSTRACT

Gas–solid momentum transfer is a fundamental problem that is characterized by the dependence of normalized average fluid–particle force F on solid volume fraction ϕ and the Reynolds number based on the mean slip velocity Re_m. In this work we report particle-resolved direct numerical simulation (DNS) results of interphase momentum transfer in flow past fixed random assemblies of monodisperse spheres with finite fluid inertia using a continuum Navier–Stokes solver. This solver is based on a new formulation we refer to as the Particle-resolved Uncontaminated-fluid Reconcilable Immersed Boundary Method (PUReIBM). The principal advantage of this formulation is that the fluid stress at the particle surface is calculated directly from the flow solution (velocity and pressure fields), which when integrated over the surfaces of all particles yields the average fluid–particle force. We demonstrate that PUReIBM is a consistent numerical method to study gas–solid flow because it results in a force density on particle surfaces that is reconcilable with the averaged two-fluid theory. The numerical convergence and accuracy of PUReIBM are established through a comprehensive suite of validation tests. The normalized average fluid–particle force F is obtained as a function of solid volume fraction ϕ ($0.1 \leqslant \phi \leqslant 0.5$) and mean flow Reynolds number Re_m ($0.01 \leqslant Re_m \leqslant 300$) for random assemblies of monodisperse spheres. These results extend previously reported results of Hill et al. (2001a,b) to a wider range of ϕ, Re_m, and are more accurate than those reported by Beetstra et al. (2007). Differences between the drag values obtained from PUReIBM and the drag correlation of Beetstra et al. (2007) are as high as 30% for Re_m in the range 100–300. We take advantage of PUReIBM's ability to directly calculate the relative contributions of pressure and viscous stress to the total fluid–particle force, which is useful in developing drag correlations. Using a scaling argument, Hill et al. (2001b) proposed that the viscous contribution is independent of Re_m but the pressure contribution is linear in Re_m (for $Re_m > 50$). However, from PUReIBM simulations we find that the viscous contribution is not independent of the mean flow Reynolds number, although the pressure contribution does indeed vary linearly with Re_m in accord with the analysis of Hill et al. (2001b). An improved correlation for F in terms of ϕ and Re_m is proposed that corrects the existing correlations in Re_m range 100–300. Since this drag correlation has been inferred from simulations of fixed particle assemblies, it does not include the effect of mobility of the particles. However, the fixed-bed simulation approach is a good approximation for high Stokes number particles, which are encountered in most gas–solid flows. This improved drag correlation can be used in CFD simulations of fluidized beds that solve the average two-fluid equations where the accuracy of the drag law affects the prediction of overall flow behavior.

1. Introduction

Gas–solid flows occur in many industrial applications such as energy generation, as well as food, chemical, and pharmaceutical processing. A fundamental understanding of gas–solid flows continues to be important, especially due to increasing interest in technologies such as carbon-neutral energy generation (Azar et al., 2006), chemical looping combustion (Shen et al., 2008), and CO_2 capture from flue gases using dry sorbents (Yi et al., 2007; Abanades et al., 2004).

Computational fluid dynamics (CFD) simulations (Syamlal et al., 1993; Kashiwa and Gaffney, 2003; Sun et al., 2007) that solve the averaged equations of multiphase flow are increasingly being used as an efficient alternative for design optimization because experiments are often costly and time-consuming. CFD simulations of multiphase flow are based on either the Lagrangian–Eulerian (LE) or the Eulerian–Eulerian (EE) two-fluid approach (Anderson and Jackson, 1967; Drew and Passman, 1998). In the EE approach that

* Corresponding author.
E-mail address: shankar@iastate.edu (S. Subramaniam).

0301-9322/$ - see front matter © 2011 Elsevier Ltd. All rights reserved.
doi:10.1016/j.ijmultiphaseflow.2011.05.010

forms the basis for popular gas–solid CFD codes (Syamlal et al., 1993; Kashiwa and Gaffney, 2003), averaged equations for mass, momentum and energy are written for both the solid and fluid phases, with coupling terms that represent interphase interactions. These coupling terms are unclosed and need to be modeled. For instance, the mean momentum conservation equation in the particle phase requires closure of the average fluid–particle interaction force (mean drag force) in terms of average quantities such as the solid volume fraction ϕ and the mean flow Reynolds number Re_m. This closure for the average fluid–particle force is popularly known as a "drag law" and is typically obtained from a combination of theoretical, experimental and computational studies.

Several studies (Bokkers et al., 2004; Benyahia et al., 2005; Leboreiro et al., 2008) point out the importance of the fluid–particle drag in determining the characteristics of monodisperse fluidized beds. Patil et al. (2005) observe that the prediction of injected bubbles in a bubbling, gas-fluidized bed operated by a jet depends on the choice of the drag law. Also, drag laws for polydisperse gas–solid suspensions are based on the drag law for an equivalent monodisperse suspension (van der Hoef et al., 2005; Beetstra et al., 2007; Yin and Sundaresan, 2009a,b; Holloway et al., 2010). Therefore, the predictive capability of CFD simulations of polydisperse gas–solid suspensions depends on the accuracy of the monodisperse drag law. Besides CFD simulations, the functional dependence of drag on volume fraction is important in the stability analysis of two-fluid equations and in predicting the stability limits of fluidized beds (Koch, 1990; Koch and Sangani, 1999).

Theoretical studies to predict the average fluid–particle force or the drag force are limited to dilute solid volume fractions and low mean flow Reynolds numbers (Stokes flow regime). Hasimoto (1959) obtained an expression for the drag force in Stokes flow past a dilute ordered arrangement of spheres by deriving periodic fundamental solutions of the Stokes equations. Later Sangani and Acrivos (1982) calculated the drag force in Stokes flow past ordered arrays of spheres over the complete range of volume fraction. In the Stokes flow regime, the Carman correlation (Carman, 1937) is widely used for packed beds of monodisperse spherical particles. At low Reynolds numbers Hill et al. (2001a) used lattice Boltzmann simulations to propose an expression for the drag force in random arrangements of spheres that is valid at all volume fractions.

At higher Reynolds numbers the nonlinearity of the governing Navier–Stokes equations together with the randomness in particle configurations make the theoretical analysis of this problem very difficult. Closures for the average fluid–particle force that are widely used in engineering practice are either obtained from pressure drop measurements in packed beds (Ergun, 1952) or measurements of terminal velocity in sedimenting suspensions (Richardson and Zaki, 1954). A limitation of these studies is that they are applicable only in the dense regime. Another closure equation for the drag force that is widely used in CFD simulations of gas–solid flow is given by Wen and Yu (1966). This drag correlation is convenient to use in CFD simulations where a range of solid volume fractions and Reynolds numbers are encountered within the computational domain. Further modifications to the Wen–Yu equation are proposed by various researchers (Gidaspow, 1986; Syamlal and O'Brien, 1987).

The exponential rise of computing power and advances in numerical methods have made it possible to perform detailed and accurate numerical simulations of flow past random particle assemblies at higher Reynolds numbers. Particle-resolved direct numerical simulation (DNS) is a first-principles approach to developing accurate models for interphase momentum transfer in gas–solids flow. Since DNS solves the governing Navier–Stokes (NS) equations with exact boundary conditions at each particle surface, it produces a model-free solution with complete three-dimensional time-dependent velocity and pressure fields.

Recently, a variety of numerical approaches have been developed for particle-resolved DNS. These can be broadly classified as those that rely on a body-fitted mesh to impose boundary conditions at particle surfaces, and those that employ regular Cartesian grids. The body-fitted methods include the arbitrary Lagrangian Eulerian (ALE) approach (Hu et al., 2001; Nomura and Hughes, 1992) as well as the method used by Balachandar and co-workers (Bagchi and Balachandar, 2003; Bagchi and Balachandar, 2004). Also Burton and Eaton (2005) used the overset grid technique to study the interaction between a fixed particle and decaying homogeneous isotropic turbulence. The principal disadvantage with approaches based on body-fitted meshes is that repeated re-meshing and solution projection are required for moving interfaces.

For methods that employ regular Cartesian grids this need for re-meshing and projection is eliminated, resulting in much faster solution times for moving particle simulations. Even for fixed particle assemblies, the wide range of parameters encountered in gas–solids flow and the need to perform multiple independent simulations (MIS) (due to the random arrangements of the particles) makes it impractical to use body-fitted meshes. However, because the grid does not conform to the particle surface, special attention is needed to generate an accurate solution. Popular methods based on regular Cartesian grids include the fictitious domain method, the lattice Boltzmann method (LBM), and the Immersed Boundary Method (IBM). The fictitious domain method with Lagrange multipliers has been developed to solve flow past many moving particles by several research groups (Patankar et al., 2000; Glowinski et al., 2001; Sharma and Patankar, 2005; Apte et al., 2009). LBM has been used to simulate flow through a fixed bed of spheres (Hill et al., 2001a,b; van der Hoef et al., 2005; Beetstra et al., 2007). and for particulate flows (Ladd and Verberg, 2001; Ten Cate et al., 2004). The immersed boundary method first proposed by Peskin (1981) is used to simulate flexible boundaries in a flow field. More recently, several researchers (Uhlmann, 2005; Yusof, 1996; Garg, 2009; Kim and Choi, 2006; Lucci et al., 2010) have modified IBM to study the interaction between flow and rigid particles. Besides these widely used techniques, there are other methods such as PHYSALIS (Oguz and Prosperetti, 2001; Takagi et al., 2005; Zhang and Prosperetti, 2003, 2005) that use a general analytic solution of the Stokes equation in the flow domain close to particle boundaries to impose the no-slip velocity boundary condition on the particle surface. In this work we describe a particle-resolved DNS methodology based on the immersed boundary method.

In order to specify a closure for the interphase momentum transfer term, it is natural to simulate a statistically homogeneous suspension flow with freely moving particles and to then compute volume-averaged estimates of the average fluid–particle force from the particle acceleration data. Imposing a pressure gradient that balances the weight of the suspension leads to a steady momentum balance. In this setup the particle positions and velocities sample a trajectory in the phase space that corresponds to the specified non-equilibrium steady state of the system. However, such freely moving suspensions are computationally prohibitive because in order to propose drag laws these simulations need to be performed over a range of solid volume fractions and mean flow Reynolds numbers. However, we note that the Stokes numbers encountered in typical gas–solid flow applications (e.g., coal particles in air) are usually very high ($\sim O(10^5)$). A convenient simplification for high Stokes number suspensions is to replace the ensemble of particle positions and velocities sampled by the system in its nonequilibrium steady state, by a set of particle configurations and velocities that would result from a granular gas simulation. Steady flow is simulated past fixed assemblies of

particles in configurations (and with velocities) sampled from this set, and drag laws are obtained by averaging over this ensemble. The idea of extracting computational drag laws from steady flow past fixed random assemblies of spheres has been successfully exploited by several researchers (Hill et al., 2001a,b; van der Hoef et al., 2005; Beetstra et al., 2007).

Hill et al. (2001a,b) referred to collectively as HKL from hereon, studied the steady flow past ordered and random arrays of monodisperse spheres. While van der Hoef et al. (2005) extended HKL's LBM simulations to account for polydispersity in the Stokes flow regime, Beetstra et al. (2007) collectively referred to as BVK from hereon, proposed a drag correlation for mono- and bi-disperse random arrays at higher Reynolds numbers. Yin and Sundaresan (2009a) proposed a new drag correlation for Stokes flow in fixed assemblies of monodisperse spheres to account for particle–particle relative motion. All the computational drag laws for flow past random arrays of spheres discussed so far are based on the lattice Boltzmann code SUSP3D developed by Ladd (1994a,b).

It is worthwhile to examine the requirements that any particle-resolved DNS approach should satisfy for specifying a closure for the average interphase momentum transfer term in gas–solids flow. One of these requirements is the consistency of the DNS approach with the two-fluid theory of multiphase flow. On each realization of a multiphase flow, the fluid stress at the particle surfaces generates a surface force density $\tau_{ji}n_j\delta(\mathbf{x}-\mathbf{x}^{(I)})$, where $\boldsymbol{\tau}$ is the fluid stress tensor and $\mathbf{n}$ is the normal vector pointing into the fluid at a point $\mathbf{x}^{(I)}$ on the particle surface. A similar term appears in the so called whole-domain formulation (Scardovelli and Zaleski, 1999). Averaging over several realizations (particle configurations) results in the expected value of the surface force density which is the average interphase momentum transfer term $\langle\tau_{ji}n_j\delta(\mathbf{x}-\mathbf{x}^{(I)})\rangle$ appearing in the two-fluid theory (Drew, 1983). Consistency of the DNS approach with two-fluid theory requires that the method used to estimate the surface force density in the DNS should be consistent with the definition of the average interphase momentum transfer term. Otherwise, the model (drag law) inferred from DNS may not be consistent with the EE equations that arise from the two-fluid theory.

In the SUSP3D code used by HKL and BVK, a spherical particle is represented by a stair-step lattice approximation and so the exact value of the particle diameter is not known *a priori*. The drag values obtained from SUSP3D simulations are assumed to correspond to an effective hydrodynamic diameter that is obtained *a posteriori* by calibrating the simulations against the analytical solution of Hasimoto (1959) for Stokes flow in a dilute simple cubic arrangement of spheres. This hydrodynamic diameter depends on the fluid viscosity as well as the particle size. So the momentum transfer at boundary lattice nodes does not correspond to the force density at the surface of the particle and the magnitude of this surface force density is calibrated. It has not been demonstrated that solutions obtained from SUSP3D reconcile with the random-field multiphase flow theory. It must be noted here that recent developments in LBM have removed the need for calibrating the hydrodynamic diameter (Ginzburg et al., 2003).

Another requirement of a particle-resolved DNS approach is to ensure that the simulation approach results in grid independent solutions. If we take steady incompressible flow past a single particle at a specified Re_m, then the flow solution and drag force should converge as the grid is progressively refined. It is not established by HKL or BVK that for a given physical problem corresponding to a fixed Re_m and fixed level of compressibility their simulations result in numerically converged solutions as the lattice spacing is reduced progressively.

In any particle-resolved DNS approach, the grid resolution should be increased with increasing Reynolds number to properly resolve the boundary layers as the boundary layer thickness $\delta \sim D/\sqrt{\mathrm{Re}_m}$. Respecting the resolution restrictions of LBM, HKL simulated only unto a Reynolds number of 100 and progressively refined their grid with increasing Reynolds numbers. However, BVK used a constant grid resolution of 21.5 lattice units to simulate Reynolds numbers ranging from 21 to 1000 at a given volume fraction while the boundary layer thickness δ reduces by 30-fold. Clearly, the boundary layers cannot be resolved at this resolution.

Besides consistency and numerical convergence, it is necessary to ensure that the simulation setup using which the drag law is inferred corresponds to a Galilean–Invariant (GI) transformation of the original physical problem. Moreover, any DNS code used to infer the drag law should ensure that the total fluid–particle force obtained by solving the physical problem in various GI simulation setups should be the same. We discuss the various GI simulation setups to extract computational drag laws in Section 7 and show that PUReIBM gives the same solution for all GI setups. We also show that using a non-GI simulation setup leads to erroneous results and these errors are compounded with increasing Reynolds numbers.

In this work, we study the flow past fixed random assemblies of monodisperse spheres using a Particle-resolved Uncontaminated-fluid Reconcilable Immersed Boundary Method (PUReIBM). We present a comprehensive set of drag data for monodisperse gas–solid suspensions using an incompressible NS solver. In PUReIBM the flow solution is obtained on a structured Cartesian grid, but the particle surface is discretized in spherical coordinates and the total force exerted by the fluid on the particle is computed directly from the stress tensor at the particle surface. This feature enables us to compare the DNS solution with any random-field theory of multiphase flow. In Section 2 we derive the ensemble-averaged two-fluid equations and in Section 3 we show that the numerical equations solved in PUReIBM are consistent and can be reconciled with the equations of two-fluid theory. We describe the simulation methodology and the relevant numerical parameters in Section 4. In Section 5 we establish the spatial and temporal convergence of PUReIBM solutions. The PUReIBM solver is validated for several test cases in Section 6. We compare various Galilean Invariant simulation setups that can be used to extract computational drag laws in Section 7 and show that PUReIBM results in a Galilean Invariant solution to the physical problem of flow past a fixed assembly of spheres. In Section 8.1 we compare the average fluid–particle force and the velocity and pressure fields obtained from PUReIBM simulation of flow past a random configuration of spheres ($\phi = 0.4$ and $\mathrm{Re}_m = 100$) with those obtained from solving the same problem with a body-fitted grid using the ANSYS-FLUENT CFD package.

As discussed earlier, in PUReIBM the force acting on the sphere is computed by integrating the pressure and viscous stresses separately over the particle surface and it is possible to investigate their relative contributions to the drag force. In Section 8.2 we discuss the normalized pressure and viscous contributions to the total drag and their dependence on volume fraction and mean flow Reynolds number. We also investigate the local profiles of pressure and viscous forces along the surface of the sphere. A new correlation for the average fluid–particle force in random arrays of monodisperse spheres is presented in Section 9. Finally, Section 10 summarizes the principal findings of this work.

2. Governing equations

A schematic describing the problem of flow past a random assembly of particles is shown in Fig. 1. For incompressible flows, the mass and momentum conservation equations for the fluid-phase are

$$\frac{\partial u_i}{\partial x_i} = 0, \tag{1}$$

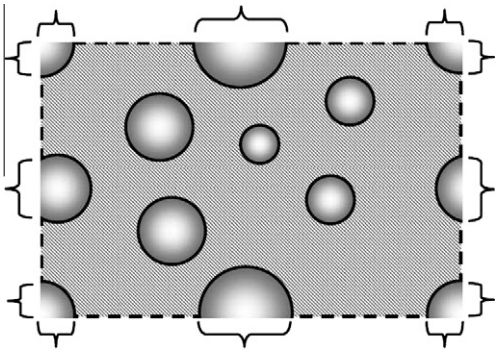

Fig. 1. A schematic of a realization of gas-solid flow showing a statistically homogeneous assembly of particles in a representative region $\mathcal{V}$, bounded by surface $\partial\mathcal{V}$. The region $\mathcal{V}$ is composed of the region $\mathcal{V}_f$ occupied by the fluid phase that is bounded by the surface $\partial\mathcal{V}_f$, and the region $\mathcal{V}_s$ occupied by the solid phase that is bounded by the surface $\partial\mathcal{V}_s$, such that $\mathcal{V} = \mathcal{V}_s \cup \mathcal{V}_f$. The boundary $\partial\mathcal{V}$ is decomposed as $\partial\mathcal{V} = \partial\mathcal{V}_s^{ext} \cup \partial\mathcal{V}_f^{ext}$, where $\partial\mathcal{V}_s^{ext} = \partial\mathcal{V} \cap \partial\mathcal{V}_s$ (shown by curly braces) is the domain boundary cut by the solid particles, and $\partial\mathcal{V}_f^{ext} = \partial\mathcal{V} \cap \partial\mathcal{V}_f$ (shown by dashed lines) is the remaining domain boundary. The boundary of the solid–phase can be expressed as the union of external and internal boundaries $\partial\mathcal{V}_s = \partial\mathcal{V}_s^{ext} \cup \partial\mathcal{V}^{int}$, where $\partial\mathcal{V}^{int}$ (shown by solid lines) is the bounding surface of the solid particles in contact with the fluid. Similarly, the boundary of the fluid–phase can be expressed as $\partial\mathcal{V}_f = \partial\mathcal{V}_f^{ext} \cup \partial\mathcal{V}^{int}$.

and

$$\rho_f \frac{\partial u_i}{\partial t} + \rho_f \frac{\partial u_i u_j}{\partial x_j} = -g_i + \frac{\partial \tau_{ji}}{\partial x_j}, \tag{2}$$

respectively, where ρ_f is the thermodynamic density of the fluid-phase. In (2), $\mathbf{g}$ represents body forces (e.g., hydrostatic pressure gradient or acceleration due to gravity) acting throughout the volume of an infinitesimal fluid element, while $\boldsymbol{\tau}$ represents the surface stresses (both pressure and viscous stresses) acting on the surface of an infinitesimal fluid element, so that

$$\frac{\partial \tau_{ji}}{\partial x_j} = -g_i' + \mu_f \frac{\partial^2 u_i}{\partial x_j \partial x_j}, \tag{3}$$

where μ_f is the dynamic viscosity of the fluid and $\mathbf{g}'$ is the gradient in the pressure acting on the surface of a fluid element. At the particle–fluid interface, the no-slip and no-penetration (for impermeable surfaces) boundary conditions require the relative velocity between fluid and solid to be zero. We note that Eqs. (1) and (2) together with the boundary conditions are true for a single realization of a gas–solid flow, and are valid only in the region $\mathcal{V}_f$ occupied by the fluid.

It is worthwhile to derive equations that are valid in the whole region $\mathcal{V}$ because such equations are the starting point for the derivation of ensemble-averaged equations. Since particle-resolved DNS methods that employ Cartesian grids solve the governing equations in the entire computational domain, we can relate the numerical formulation with the governing equations that are valid in the entire physical domain.

The momentum conservation equation valid in the entire domain is obtained by multiplying Eq. (2) by the fluid-phase indicator function $I_f(\mathbf{x},t)$ which is unity if the point $\mathbf{x}$ lies in the fluid-phase and zero otherwise. The indicator function obeys the topological equation (Drew, 1983):

$$\frac{\partial I_f}{\partial t} + U_j^{(I)} \frac{\partial I_f}{\partial x_j} = 0, \tag{4}$$

where $\mathbf{U}^{(I)}$ is the velocity of the fluid–particle interface. This equation simply states that the indicator function is convected by the velocity of the fluid–particle interface. Using the topological Eq. (4) and multiplying (2) with I_f one obtains:

$$\rho_f \frac{\partial I_f u_i}{\partial t} + \rho_f \frac{\partial I_f u_i u_j}{\partial x_j} = -I_f g_i + \rho_f u_i (u_j - U_j^{(I)}) \frac{\partial I_f}{\partial x_j} + \frac{\partial I_f \tau_{ji}}{\partial x_j} - \tau_{ji} \times \frac{\partial I_f}{\partial x_j}. \tag{5}$$

The second term on the right hand side of (5) represents momentum source due to the difference between the interface velocity and the velocity of the fluid at the fluid–particle interface, which occurs in two-phase flows with interphase mass transfer, e.g. vaporization. Since we consider gas–solids flow with no mass transfer at the interface, this term is zero. The gradient of the indicator function $\partial I_f / \partial x_j$ can be expressed as $-n_j^{(f)} \delta(\mathbf{x} - \mathbf{x}^{(I)})$ (Drew, 1983), where $\mathbf{n}^{(f)}$ is the unit normal vector pointing outward from the fluid surface into the particle, and $\delta(\mathbf{x} - \mathbf{x}^{(I)})$ is a generalized delta function[1] at the fluid–particle interface $\mathbf{x}^{(I)}$. Substituting the definition of the gradient of the indicator function into (5), the momentum conservation equation valid in the entire domain is:

$$\rho_f \frac{\partial I_f u_i}{\partial t} + \rho_f \frac{\partial I_f u_i u_j}{\partial x_j} = -I_f g_i + \frac{\partial I_f \tau_{ji}}{\partial x_j} - \tau_{ji} n_j^{(s)} \delta(\mathbf{x} - \mathbf{x}^{(I)}). \tag{6}$$

In the above equation $\mathbf{n}^{(s)}$ is the normal vector pointing outward from the particle surface into the fluid, i.e., $\mathbf{n}^{(s)} = -\mathbf{n}^{(f)}$. The last term on the right hand side of (6), namely, $-\tau_{ji} n_j^{(s)} \delta(\mathbf{x} - \mathbf{x}^{(I)})$, is the surface force density and it represents momentum transfer at the fluid–particle interface. We will show in the following section that the average of the surface force density appears as an unclosed term in the ensemble-averaged equations that can be quantified by particle-resolved DNS. Eq. (6) is similar to the momentum conservation equation solved in the whole-domain formulation of Scardovelli and Zaleski (1999). There are several ways to solve (6) and particle-resolved DNS methodologies differ in the procedure used to compute the surface force density. We now derive the ensemble-averaged two-fluid equations corresponding to mass and momentum conservation and identify the unclosed terms.

2.1. Ensemble-averaged two-fluid equations

In the Eulerian two-fluid theory, phasic averages are defined as averages conditional on the presence of fluid or solid phase. If $Q(\mathbf{x},t)$ is any field, then its phasic average $\langle Q^{(f)} \rangle(\mathbf{x},t)$ referred to as its fluid-phase mean, is defined as:

$$\langle Q^{(f)} \rangle(\mathbf{x},t) = \frac{\langle I_f(\mathbf{x},t) Q(\mathbf{x},t) \rangle}{\langle I_f(\mathbf{x},t) \rangle}, \tag{7}$$

where I_f is the indicator function described earlier. The solid-phase mean $\langle Q^{(s)} \rangle(\mathbf{x},t)$ is similarly defined.

The mean momentum conservation equation in the fluid phase (Drew, 1983; Pai and Subramaniam, 2009) can be derived by ensemble-averaging (6) resulting in

$$\frac{\partial}{\partial t}\left\{\rho_f(1-\phi)\left\langle u_i^{(f)}\right\rangle\right\} + \frac{\partial}{\partial x_j}\left\{\rho_f(1-\phi)\left\langle u_i^{(f)}\right\rangle\left\langle u_j^{(f)}\right\rangle\right\} = -(1-\phi)\left\langle g_i^{(f)}\right\rangle - \frac{\partial}{\partial x_j}\left\{\rho_f\left\langle I_f u_i''^{(f)} u_j''^{(f)}\right\rangle\right\} + \left\langle \frac{\partial I_f \tau_{ji}}{\partial x_j}\right\rangle - \left\langle \tau_{ji} n_j^{(s)} \delta(\mathbf{x} - \mathbf{x}^{(I)})\right\rangle, \tag{8}$$

where $u_i''^{(f)} = u_i - \left\langle u_i^{(f)}\right\rangle$ denotes the fluctuations in the fluid veloc-

[1] The generalized delta function $\delta^{(d),(k)}(\mathbf{x} - \mathbf{x}^{(I)})$ allows the representation in $\mathcal{R}^{(d)}$ of quantities defined in $\mathcal{R}^{(k)}, k < d$. The dimensions of the generalized delta functions are L^{k-d}. In this case $d = 3$ and $k = 2$, so the delta function has dimensions L^{-1} and hence it allows the surface force density to be written as an interphase momentum transfer term in $\mathcal{R}^{(3)}$.

ity field with respect to the phase-averaged fluid velocity and $\phi = \langle I_s \rangle$ is the average volume fraction of the solid phase and $(1-\phi)$ is the average volume fraction of the fluid phase. The terms on the right hand side are the average body force density, the transport of fluid-phase velocity fluctuations, and the average interphase momentum transfer respectively, of which the last two are the unclosed terms that need to be modeled.

In this work we perform particle-resolved DNS of statistically homogeneous suspensions to model the average interphase momentum transfer. For a statistically homogeneous suspension the average quantities do not depend on $\mathbf{x}$ and hence the convective term on the left hand side of (8), and the transport of fluid-phase velocity fluctuations on the right hand side are zero. Therefore, the phasic averaged fluid velocity evolves as:

$$\frac{\partial}{\partial t}\left\{\rho_f(1-\phi)\left\langle u_i^{(f)}\right\rangle\right\} = -(1-\phi)\left\langle g_i^{(f)}\right\rangle - \left\langle \tau_{ji} n_j^{(s)} \delta(\mathbf{x}-\mathbf{x}^{(l)})\right\rangle. \tag{9}$$

The mean fluid velocity reaches a steady state when the average interphase momentum transfer balances the body forces like gravity or an imposed pressure gradient:

$$(1-\phi)\left\langle g_i^{(f)}\right\rangle = -\left\langle \tau_{ji} n_j^{(s)} \delta(\mathbf{x}-\mathbf{x}^{(l)})\right\rangle. \tag{10}$$

As noted earlier $\left\langle \tau_{ji} n_j^{(s)} \delta(\mathbf{x}-\mathbf{x}^{(l)})\right\rangle$ is the unclosed average interphase momentum transfer. We now describe how this quantity can be computed from solution of flow past statistically homogeneous suspensions using particle-resolved DNS.

2.2. Quantifying average interphase momentum transfer from particle-resolved DNS

In particle-resolved DNS, a statistically homogeneous suspension is approximated by flow past a random configuration of particles in a periodically repeating unit cell. Let $\mathbf{u}(\mathbf{x},t;\omega)$ be the velocity field obtained from particle-resolved DNS of flow past a random configuration of particles represented by the positions and velocities $\{\mathbf{X}^{(i)},\mathbf{V}^{(i)}, i = 1,\ldots,N_p\}$ of N_p particles. This configuration represents a realization ω in the sample space Ω of all possible configurations. The ensemble-averaged velocity field or the mathematical expectation is defined as (Subramaniam, 2000):

$$\langle \mathbf{u} \rangle(\mathbf{x},t) = \int_\Omega \mathbf{u}(\mathbf{x},t;\omega) dP_\omega, \tag{11}$$

where P_ω is the probability measure that is defined on Ω. If the flow is statistically homogeneous, ensemble-averaged quantities can be approximated by taking the volumetric mean of the solution fields, e.g. the volumetric mean of the velocity field over the fluid region is defined as:

$$\langle \mathbf{u}^{(f)} \rangle_{\mathcal{V}}(t;\omega) = \frac{1}{V_f}\int_{\mathcal{V}} I_f(\mathbf{x},t;\omega)\mathbf{u}(\mathbf{x},t;\omega) dV, \tag{12}$$

where V_f is the volume of the region occupied by the fluid-phase. The volumetric mean approaches the ensemble average in the limit of infinite box size (i.e., $V \to \infty$). A reasonable approximation is obtained with finite box size provided the two-point correlations in the particle and the fluid phases decay to zero within the box length.[2] However, in order to account for the statistical variability arising from different particle configurations, we require very large box sizes. Especially for dilute suspensions, since average quantities in the particle phase (such as the average fluid–particle force) converge to their expected values as $1/\sqrt{N_P}$, this requirement can be computationally prohibitive. In order to accurately estimate the ensemble-averaged interphase momentum transfer from finite box sizes, two approaches are available: (i) simulate freely evolving suspensions and use time-averaging to calculate estimates for statistically stationary flows or, (ii) simulate fixed particle assemblies and average over different configurations. The choice of approach depends on the nature of the problem.

For fixed particle assemblies, the ensemble-average can be estimated by averaging over different configurations or realizations, i.e.,

$$\{\mathbf{u}^{(f)}\}_{\mathcal{V},\mathcal{M}}(t) = \frac{1}{\mathcal{M}}\sum_{\mu=1}^{\mathcal{M}} \langle \mathbf{u}^{(f)} \rangle_{\mathcal{V}}(t;\omega_\mu). \tag{13}$$

In the above equation $\{\mathbf{u}^{(f)}\}_{\mathcal{V},\mathcal{M}}$ denotes an estimate of the true expectation $\langle \mathbf{u}^{(f)} \rangle$ and $\mathcal{M}$ denotes the number of independent configurations. For freely evolving suspensions of statistically stationary flow, the ensemble-averaged quantities can be estimated using time-averaging:

$$\{\mathbf{u}^{(f)}\}_{\mathcal{V},T} = \frac{1}{T}\int_{t_0}^{t_0+T} \langle \mathbf{u}^{(f)} \rangle_{\mathcal{V}}(t'); dt'. \tag{14}$$

In either case, the evolution equation for the volumetric mean fluid velocity can be derived by integrating (6) over the entire region $\mathcal{V}$ to obtain:

$$\begin{aligned}\rho_f V_f \frac{d\left\langle u_i^{(f)}\right\rangle_{\mathcal{V}}}{dt} + \rho_f \oint_{\partial\mathcal{V}} (I_f u_i u_j) n_j \, dA \\ = -V_f\left\langle g_i^{(f)}\right\rangle_{\mathcal{V}} + \oint_{\partial\mathcal{V}} (I_f \tau_{ji}) n_j \, dA - \oint_{\partial\mathcal{V}^{\text{int}}} \tau_{ji} n_j^{(s)} \, dA,\end{aligned} \tag{15}$$

where $\mathbf{n}$ is the unit outward normal vector to the domain. In deriving the above equation, we used the Gauss-divergence theorem and properties of the gradient of the indicator function (Drew, 1983). The second term on the left hand side denotes the net convective flux entering the domain while the second term on the right hand side side denotes the net diffusive flux and surface pressure acting on the domain. Due to periodic boundaries these terms are zero. Thus the conservation of momentum averaged over the fluid region reads:

$$\rho_f(1-\phi)\frac{d\left\langle u_i^{(f)}\right\rangle_{\mathcal{V}}}{dt} = -(1-\phi)\left\langle g_i^{(f)}\right\rangle_{\mathcal{V}} - \frac{1}{V}\oint_{\partial\mathcal{V}^{\text{int}}} \tau_{ji} n_j^{(s)} dA. \tag{16}$$

In writing this equation we used the property that for a statistically homogeneous suspension, the volume fraction of the fluid phase is given by $(1-\phi) = V_f/V$. The volumetric mean fluid velocity attains a steady value when the surface stresses acting on the fluid–particle interface balance the body forces, i.e.,

$$(1-\phi)\left\langle g_i^{(f)}\right\rangle_{\mathcal{V}} = -\frac{1}{V}\oint_{\partial\mathcal{V}^{\text{int}}} \tau_{ji} n_j^{(s)} dA. \tag{17}$$

Eq. (17) is the DNS counterpart of the ensemble-averaged momentum balance (10), and it is clear that under the assumption of statistical homogeneity the average interphase momentum transfer term can be estimated using the volumetric mean of surface stresses. We now describe how this momentum balance is accomplished for flow past fixed particle assemblies neglecting the effect of gravity. The corresponding formulation for flow past freely evolving gas–solid suspensions has been discussed by Tenneti et al. (2010).

2.3. Fixed particle assemblies

There are two approaches to set up the problem of flow past fixed particle assemblies. We can impose a constant pressure gradient across the domain, in which case, $\langle \mathbf{g}^{(f)} \rangle_{\mathcal{V}}$ is known *a pri-*

[2] This is simply the two-phase extension of the criterion given by Pope (2000) for single-phase turbulent flows.

ori and the volume-averaged fluid velocity evolves to reach a steady state corresponding to the imposed pressure gradient. Another approach is to specify a desired volumetric flow rate and the volume-averaged pressure gradient $\langle \mathbf{g}^{(f)} \rangle_{\mathcal{V}}$ is adjusted to maintain the specified flow rate. The physical problem corresponding to both these approaches can be simulated in any particle-resolved DNS methodology. Hill et al. (2001b) proposed their LBM-based drag correlation by imposing a known constant pressure gradient. In our simulations using PUReIBM DNS, we specify the desired flow rate and obtain the pressure gradient as an output. In the following section we describe the governing equations in our numerical method and show that the volume-average estimate of the average interphase momentum transfer obtained from the simulations is consistent with the two-fluid theory.

3. Solution approach

In PUReIBM, we employ Cartesian grids and solve the mass and momentum conservation equations at all the grid points (including those lying inside the particles). A fictitious flow is generated inside the particles that does not affect the exterior flow solution. The mass and momentum conservation equations that are solved in PUReIBM are

$$\frac{\partial u_i}{\partial x_i} = 0, \tag{18}$$

and

$$\rho_f \frac{\partial u_i}{\partial t} + \rho_f S_i = -g_{\mathrm{IBM},i} + \mu_f \frac{\partial^2 u_i}{\partial x_j \partial x_j} + f_{\mathrm{u},i}, \tag{19}$$

respectively, where $\mathbf{g}_{\mathrm{IBM}}$ is the pressure gradient, $\mathbf{S} = \nabla \cdot (\mathbf{uu})$ is the convective term in conservative form, and $\mathbf{u}$ is the instantaneous velocity field. In the momentum conservation equation (cf. (19)), $\mathbf{f}_{\mathrm{u}}$ is the additional immersed boundary (IB) force term that accounts for the presence of solid particles in the fluid-phase by ensuring the no-slip and no-penetration boundary conditions at the particle–fluid interface.

The surface of the solid particle is represented by a discrete number of points called boundary points. For spherical particles, the boundary points are specified by discretizing the sphere in spherical coordinates. In Fig. 2, a schematic describing the computation of the IB forcing is shown for the equatorial plane passing through the spherical particle. Another set of points called exterior points are generated by projecting these boundary points onto a sphere of radius $r + \Delta r$, where r is the radius of the particle (see exterior point represented by an open circle on the dashed line in Fig. 2). Similarly, the boundary points are projected onto a smaller sphere of radius $r - \Delta r$ and these points are called interior points. In our simulations Δr is taken to be same as the grid spacing. The IB force is computed at the interior points. At these points the fluid velocity is forced in a manner similar to the ghost cell approach used in standard finite-difference/finite-volume based methods (Patankar, 1980). Specifically for the case of zero solid particle velocity, the velocity at the interior points is forced to be equal in magnitude but opposite in direction to the fluid velocity at the corresponding exterior points. Velocities at the exterior and interior points are obtained by interpolating the velocities from the neighboring grid nodes. The computation of IB forcing is similar to the direct forcing method proposed by Yusof (1996). The IB forcing at the $n+1$th time-step is specified to cancel the remaining terms in the momentum conservation, and to force the velocity to its desired value $\mathbf{u}^d$ at the interior points:

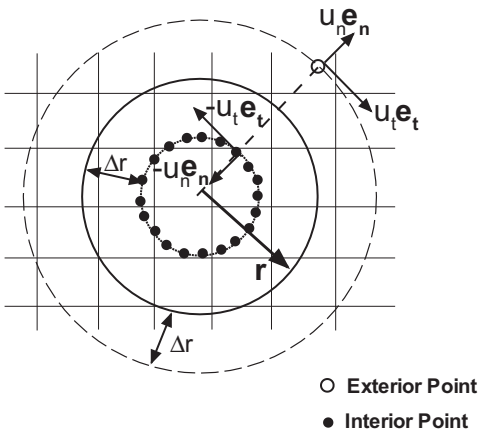

Fig. 2. A schematic showing the computation of the immersed boundary forcing for a stationary particle. The solid circle represents the surface of the particle at r. Open circle shows the location of one exterior point at $r + \Delta r$ (only one exterior point is shown for clarity, although there is one exterior point for each interior point) and filled circles show the location of interior points at $r - \Delta r$ where the immersed boundary forcing is computed. For the special case of a stationary particle, the velocity at the interior points is forced to be the opposite of the velocity at the corresponding exterior points. In the schematic, $u_n \mathbf{e}_n$ represents the normal velocity and $u_t \mathbf{e}_t$ represents the tangential velocity at the exterior point.

$$f_{\mathrm{u},i}^{n+1} = \rho_f \frac{u_i^d - u_i^n}{\Delta t} + \rho_f S_i^n + g_{\mathrm{IBM},i}^n - \mu_f \frac{\partial^2}{\partial x_j \partial x_j} u_i^n. \tag{20}$$

The IB forcing at the interior points is then interpolated to the neighboring grid nodes that do not include grid nodes in the fluid phase. It is noteworthy that the discretization of the sphere in spherical coordinates is independent of the grid resolution. To some extent this decouples the grid resolution from the accuracy with which the boundary condition is imposed.

The distinctive feature of PUReIBM is that the surface force density is directly calculated from the surface values of the velocity and pressure fields obtained from the unmodified Navier–Stokes equations in the fluid phase. This feature of PUReIBM distinguishes it from the so-called diffuse interface methods (Uhlmann, 2005; Yusof, 1996) where the IB forcing is computed on the surface of the particle and then interpolated to the neighboring grid nodes that could also lie in the fluid-phase. They are called diffuse-interface methods because the surface force density is smeared into the fluid-phase.

The governing equations in PUReIBM (cf. (18) and (19)) are solved by imposing periodic boundary conditions on fluctuating variables that are now defined. The velocity field is decomposed into a spatially uniform mean flow that is purely time-dependent, and a fluctuating velocity field $\mathbf{u}'$ that is periodic, i.e.,

$$\mathbf{u}(\mathbf{x}, t) = \langle \mathbf{u} \rangle_{\mathcal{V}}(t) + \mathbf{u}'(\mathbf{x}, t), \tag{21}$$

where the volumetric mean velocity

$$\langle \mathbf{u} \rangle_{\mathcal{V}}(t) = \frac{1}{V} \int_{\mathcal{V}} \mathbf{u}(\mathbf{x}, t) d\mathcal{V}, \tag{22}$$

is obtained by averaging the velocity field over the entire computational domain. Similar decompositions can be written for the nonlinear term $\mathbf{S}$, pressure gradient $\mathbf{g}$, and immersed boundary forcing $\mathbf{f}_{\mathrm{u}}$ terms. Substituting the above decompositions in the mass (cf. (18)) and momentum (cf. (19)) conservation equations, followed by averaging over the entire computational domain yields the volume averaged mass and momentum conservation equations. Since the volumetric means are independent of spatial location, mean mass conservation is trivially satisfied. The mean momentum conservation equation in the whole domain becomes

$$\rho_f \frac{d\langle u_i\rangle_{\mathcal{V}}}{dt} = -\langle g_{\mathrm{IBM},i}\rangle_{\mathcal{V}} + \langle f_{\mathrm{u},i}\rangle_{\mathcal{V}}, \tag{23}$$

where the volume integrals of convective and diffusive terms are zero because of periodic boundary conditions. The mean IB forcing term $\langle \mathbf{f}_{\mathrm{u}}\rangle_{\mathcal{V}}$ is computed by volume-averaging the IB force specified by (20) over the region $\mathcal{V}$. As noted earlier, the mean pressure gradient $\langle \mathbf{g}_{\mathrm{IBM}}\rangle_{\mathcal{V}}$ is computed such that we obtain the desired flow rate.

While mean mass conservation is trivially satisfied, the fluctuating velocity field needs to be divergence free, i.e.,

$$\frac{\partial u_i'}{\partial x_i} = 0. \tag{24}$$

Subtracting the mean momentum conservation Eq. (23) from the instantaneous momentum conservation Eq. (19) yields the following equation for the fluctuating velocity:

$$\rho_f \frac{\partial u_i'}{\partial t} + \rho_f S_i' = -g_i' + \mu_f \frac{\partial^2 u_i'}{\partial x_j \partial x_j} + f_{\mathrm{u},i}'. \tag{25}$$

Taking the divergence of the above equation and using Eq. (24) results in the following modified Poisson equation for the fluctuating pressure gradient:

$$\frac{\partial g_{\mathrm{IBM},i}'}{\partial x_i} = \frac{\partial f_{\mathrm{u},i}'}{\partial x_i} - \rho_f \frac{\partial S_i'}{\partial x_i}. \tag{26}$$

The conservation Eqs. (23)–(26) are solved at every grid point (including those inside the solid particles) to yield the flow around immersed bodies that satisfies the no-slip and no-penetration boundary conditions. In the following section we derive the evolution equation for the velocity averaged over the fluid-phase using the PUReIBM governing equations and show that PUReIBM is reconcilable with the two-fluid theory.

3.1. Conservation of mean momentum in the fluid-phase

The mean momentum conservation equation in the fluid-phase is derived by averaging the PUReIBM momentum conservation equation (cf. (19)) over the fluid region. When performing volume-averaging one has to account for discontinuities in the stresses at the particle–fluid interfaces. The conservation of fluid-phase mean momentum reads (see Appendix A for a detailed derivation):

$$\rho_f(1-\phi)\frac{d\left\langle u_i^{(f)}\right\rangle_{\mathcal{V}}}{dt} = -(1-\phi)\langle g_{\mathrm{IBM},i}\rangle_{\mathcal{V}} - \frac{1}{V}\oint_{\partial\mathcal{V}^{\mathrm{int}}} \tau_{ji} n_j^{(s)} dA. \tag{27}$$

We can see that the above equation is identical to (16) and thus we conclude that PUReIBM is consistent with the two-fluid theory. Note that when we average the PUReIBM momentum conservation equation (cf. (19)) over the fluid region, the average of IB forcing over the fluid region is zero since the IB forcing is non-zero only inside the particles. In IBM implementations where the IB forcing is finite in the fluid-phase (Yusof, 1996; Uhlmann, 2005), an extra term in the form of fluid-phase volume average of the IB forcing $\left\langle \mathbf{f}_u^{(f)}\right\rangle_{\mathcal{V}}$ will appear in (27).

The mean pressure gradient $\langle \mathbf{g}_{\mathrm{IBM}}\rangle_{\mathcal{V}}$ required to obtain a desired fluid-phase mean velocity $\langle \mathbf{u}^{(f)}\rangle_{\mathcal{V}}^d$, is computed using an explicit time discretization of (27) such that at the nth time step the mean pressure gradient is given by

$$-\langle \mathbf{g}_{\mathrm{IBM}}\rangle_{\mathcal{V}}^n = \rho_f \frac{\langle \mathbf{u}^{(f)}\rangle_{\mathcal{V}}^d - \langle \mathbf{u}^{(f)}\rangle_{\mathcal{V}}^n}{\Delta t} + \frac{1}{(1-\phi)V}\left\{\oint_{\partial\mathcal{V}^{\mathrm{int}}} \tau_{ji}^{(n)} n_j^{(s)}\right\} dA, \tag{28}$$

where all quantities in the integrand are evaluated on the fluid side of the fluid–particle interface, and the superscript n implies the relevant quantities at the nth time step. This equation is obtained by requiring that $\langle \mathbf{u}^{(f)}\rangle_{\mathcal{V}}^{n+1} = \langle \mathbf{u}^{(f)}\rangle_{\mathcal{V}}^d$, so that the first term on right hand side drives the volume-averaged mean fluid velocity to its desired value. The equations (23)–(26) are evolved in time until the volume-averaged quantities reach a steady state, at which point the first term on the right hand side of (28) is negligible, and consequently (28) reduces to the numerical counterpart of (17). This establishes that the resulting numerical solution to the PUReIBM governing equations is a valid numerical solution to steady flow past homogeneous particle assemblies.

The numerical scheme used in PUReIBM is a primitive-variable, pseudo-spectral method, using a Crank-Nicolson scheme for the viscous terms, and an Adams-Bashforth scheme for the convective terms. A fractional time-stepping method that is based on Kim and Moin's approach (Kim and Moin, 1985) is used to advance the velocity and pressure fields in time. Kim and Moin's algorithm involves a predictor step followed by a corrector step. The velocity field obtained from the predictor step need not be divergence free. Therefore, a corrector step is required so that the velocity is divergence free. Since PUReIBM uses this approach, the maximum divergence of the velocity field obtained at any time step is of the order of machine precision. A common criticism of this method is that due to the divergence correction the corrected velocity field does not satisfy the desired boundary condition (Muldoon and Acharya, 2008). Although the divergence correction changes the velocity of the particle surface at every time step, the velocity correction at steady state is of the order of 10^{-10}. Therefore, once steady state is reached the fluid velocity at the particle surface does not change at all. In our simulations, the maximum difference between the corrected surface velocity and the desired boundary velocity at steady state is found to be less than 10^{-3}. Since only steady flows are considered in this work, it suffices to ensure that the velocity field obeys the continuity equation. The numerical method described in this work must be modified appropriately to obtain time-accurate solutions for unsteady flows.

4. Simulation methodology

We now describe how the mean flow Reynolds number and solid volume fraction are specified in the simulation. For flow past homogeneous particle assemblies, a Reynolds number based on the magnitude of mean slip velocity between the two phases is defined as

$$\mathrm{Re}_m = \frac{|\langle \mathbf{W}\rangle|(1-\phi)D}{\nu_f}, \tag{29}$$

where $|\langle \mathbf{W}\rangle| = |\langle \mathbf{u}^{(f)}\rangle - \langle \mathbf{u}^{(s)}\rangle|$ is the magnitude of the mean slip velocity, D is the particle diameter, and $\langle \mathbf{u}^{(f)}\rangle$ and $\langle \mathbf{u}^{(s)}\rangle$ are the mean velocities in the fluid and solid phases respectively. For the purpose of generating drag correlations it is more convenient to specify the mean flow Reynolds number as input to the simulations, rather than the mean pressure gradient. For fixed particle assemblies $\langle \mathbf{u}^{(s)}\rangle = 0$ and the desired fluid-phase mean velocity $\langle \mathbf{u}^{(f)}\rangle$ is known in terms of the input Reynolds number and other physical properties.

Particles are initialized corresponding to a specified mean solid volume fraction ϕ. For ordered arrays (where a unit cell is simulated) this is accomplished by simply varying the ratio of the computational box length L to the particle diameter D. For random assemblies, the particles are fixed in a random equilibrium configuration they attain following elastic collisions (in the absence of ambient fluid) starting from a lattice arrangement with a Maxwellian velocity distribution. The elastic collisions are simulated using a soft-sphere discrete element model (Cundall and Strack, 1979; Garg et al., 2010). The pair correlation function at equilibrium specifies the particle configuration for random assemblies.

4.1. Numerical parameters

The computational domain used is a cube with sides of length L that is discretized using a regular Cartesian grid with M grid cells in each direction so that $\Delta x = L/M$ is the size of each grid cell. The spatial resolution is represented by the number of grid cells across the diameter of a particle, which is denoted $D_m = D/\Delta x$. For ordered arrays the ratio of computational box length L to the particle diameter D is not an independent parameter since L corresponds to a unit cell of the lattice arrangement and is determined by the volume fraction ϕ. Thus D_m is the only relevant numerical parameter in the simulations of ordered arrays.

For random arrays, the ratio L/D is an independent parameter. The minimum box length is determined by the criterion that the spatial autocorrelation of flow statistics must decay to zero within the box. This is to prevent the periodicity of the numerical solution from leading to unphysical flow fields. The numerical parameter L/D also determines the number of particles N_p in the box such that for a given volume fraction ϕ it is given by

$$N_p = \frac{6\phi}{\pi}\left(\frac{L}{D}\right)^3. \tag{30}$$

The number of grid cells M along each axis of the computational box determines the computational cost of the problem that scales as M^3. It is related to the grid resolution parameter D_m and the box length to particle diameter ratio, L/D as follows:

$$M = \frac{L}{\Delta x} = \frac{L}{D} D_m. \tag{31}$$

This relation shows that for fixed computational cost, there is a tradeoff between spatial resolution and box size which determines the effect of periodic boundary conditions on the numerical solution through L/D.

The solution algorithm is advanced in pseudo-time from specified initial conditions to steady state using a time step Δt that is chosen as the minimum of the convective and viscous time steps according to the criterion

$$\Delta t = \mathrm{CFL} \times \min\left\{\frac{\Delta x}{u_{\max}}, \frac{\Delta x^2(1-\phi)}{\nu_f}\right\}. \tag{32}$$

At the beginning of the simulation we set $u_{\max} = |\langle \mathbf{u}^{(f)} \rangle|$, and as the flow evolves $u_{\max}$ is set to the magnitude of the maximum fluid velocity so that the time step adapts itself to satisfy the above criterion.

Both spatial and temporal discretization contribute to numerical error in the estimation of the drag force. However, for steady flows the numerical error is determined solely by the spatial resolution parameter $\Delta x/D = 1/D_m$, which must be sufficiently small to ensure numerically converged results. The influence of these numerical parameters—the grid resolution parameter D_m, the ratio of computational box length to particle diameter L/D, and the number of solid particles N_p—on the numerical convergence of PUReIBM simulations is discussed in the next section.

4.2. Estimation of mean drag from simulations

Direct numerical simulation of flow through a particle assembly using PUReIBM results in velocity and pressure fields on a regular Cartesian grid. In PUReIBM the drag force on the ith particle, $\mathbf{F}_d^{(i)} = m^{(i)}\mathbf{A}^{(i)}$, is reported by integrating the viscous and pressure forces exerted by the fluid on the particle surface, and not from the IB forcing. The average drag force on particles in a homogeneous suspension for μth realization is computed as

$$\{\mathbf{F}_\mathrm{d}\}_\mathcal{V}^\mu = \frac{1}{N_p}\left\{-\langle \mathbf{g}_\mathrm{IBM}\rangle_\mathcal{V} V_s - \oint_{\partial\mathcal{V}_s} \psi \mathbf{dA} + \mu_\mathrm{f} \oint_{\partial\mathcal{V}_s} \nabla\mathbf{u}\cdot\mathbf{dA}\right\}. \tag{33}$$

In the above equation the first term on the right hand side is the body force due to mean pressure gradient, the second term is the drag force due to fluctuating pressure field, and the third term is the viscous contribution to the drag force. The pressure and viscous contributions to the drag force are obtained by integrating the pressure and viscous stresses over the surface of each particle. To perform this integration, the pressure and viscous stresses are interpolated to the boundary points (see Fig. 2) from the surrounding grid nodes and the force acting on the boundary point is computed by multiplying the interpolated fluid stress with the area associated with the boundary point. Summation of the forces acting on all the boundary points of the particle gives the force acting on it. The sum of the last two terms on the right hand side of Eq. (33) is the exact numerical representation of the expectation of the surface force density. Thus, we conclude that the drag law inferred from PUReIBM simulations is consistent with the two-fluid theory. It should be noted that HKL proposed their correlation for the total fluid–particle force (cf. (33)) whereas van der Hoef et al. (2005) and BVK subtracted the contribution of mean pressure gradient to propose their drag correlation.

The simulation is carried out until the average drag force per particle reaches a steady state. The difference in the drag values of successive time steps is monitored and a moving average of this difference is calculated over 10% of the time required for the fluid to travel the length of the box. If this moving average is less than a threshold (1×10^{-6} in most of the simulations), we conclude that the drag has reached its steady value. Although some unsteadiness has been observed in the velocity field particularly for volume fractions less than 0.2, there is no noticeable unsteadiness in the mean drag.

The mean drag force represents an average over all particle configurations corresponding to the same volume fraction and pair correlation function. Therefore, the drag from a single realization (cf. (33)) is averaged over multiple independent realizations (MIS) to obtain an estimate for the ensemble-averaged drag:

$$\{\mathbf{F}_\mathrm{d}\}_{\mathcal{V},\mathcal{M}} = \frac{\sum_{\mu=1}^{\mathcal{M}} \{\mathbf{F}_\mathrm{d}\}_\mathcal{V}^\mu}{\mathcal{M}}, \tag{34}$$

which converges to the true expectation of the drag force in the limit $N_p\mathcal{M} \to \infty$. The ensemble-averaged drag force is later reported as a normalized average drag force given by

$$F = \frac{\{\mathbf{F}_\mathrm{d}\}_{\mathcal{V},\mathcal{M}}}{F_\mathrm{Stokes}}, \tag{35}$$

where $F_\mathrm{Stokes} = 3\pi\mu_\mathrm{f} D(1-\phi)|\langle\mathbf{W}\rangle|$ is the Stokes drag acting on an isolated sphere moving with a slip velocity of $(1-\phi)|\langle\mathbf{W}\rangle|$. The number of multiple independent simulations $\mathcal{M}$ is determined by the requirement that the total number of samples $\mathcal{M}N_p$ in the estimate for the average force given by (34) be sufficiently large to ensure low statistical variability.

5. Numerical convergence

In this section we investigate the influence of the numerical parameters discussed in the previous section on PUReIBM simulations. We first examine the influence of the grid resolution parameter D_m and the time step Δt. We study steady flow past an ordered array of particles in a FCC lattice arrangement, because for this case the only numerical parameter is the grid resolution D_m. Although we consider steady flows, we also verify that the steady value of the drag does not change with the time step chosen to evolve the flow in pseudo time from a uniform flow initial condition.

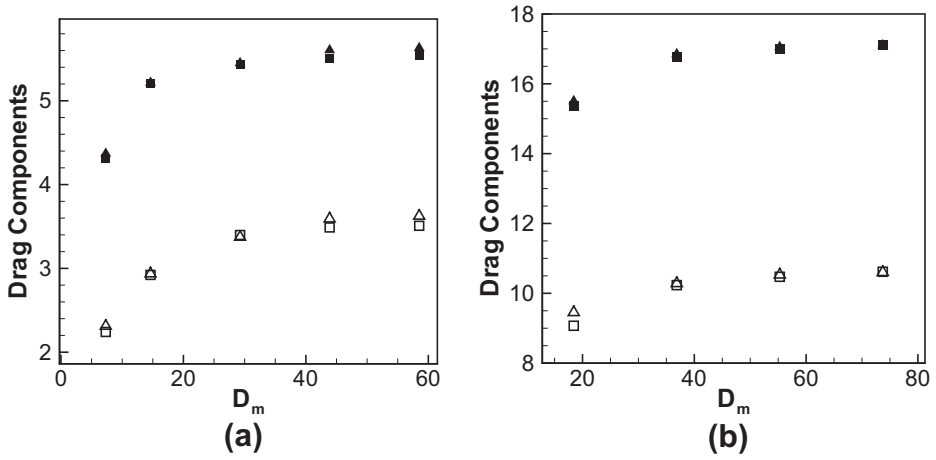

Fig. 3. Convergence characteristics of drag force due to fluctuating pressure gradient (open symbols) and viscous stresses (filled symbols) for FCC arrays at $Re_m = 40$ with grid resolution D_m for two CFL values of 0.2 (squares) and 0.05 (triangles). Volume fraction ϕ is equal to 0.2 in (a) and 0.4 in (b).

For a face centered cubic (FCC) arrangement of particles ($\phi = 0.2$, $Re_m = 40$), Fig. 3a shows the convergence characteristics of drag forces due to fluctuating pressure gradient (open symbols) and viscous stresses (filled symbols) as a function of grid resolution D_m for two different values of CFL equal to 0.2 (squares) and 0.05 (triangles). Fig. 3b shows the same convergence characteristics for a denser FCC arrangement with a solid volume fraction of 0.4 and $Re_m = 40$. In both figures it can be seen that the PUReIBM simulation result is nearly independent of the time step (CFL). The figures show that the resolution requirements increase with increasing volume fraction. We conclude that a minimum resolution of $D_m = 40$ is needed for converged results at $\phi = 0.2$, while a minimum resolution of $D_m = 60$ is required for $\phi = 0.4$. These values are based on relative error in the normalized force that can be calculated based on the normalized force values obtained on the finest grid resolution. If the relative error is less than 2%, the values are considered grid converged. Based on this criterion, $D_m = 40$ and $D_m = 60$ are considered grid converged resolutions for solid volume fractions 0.2 and 0.4, respectively. It is noted that in the simulations for ordered arrays presented in Section 6 we used much higher resolutions ($D_m = 60$ for $\phi = 0.2$; $D_m = 80$ for $\phi = 0.4$). In addition to the dependence of grid resolution on volume fraction, higher mean flow Reynolds numbers require progressively higher grid resolution. Fig. 4 shows the convergence characteristics for FCC arrays at a volume fraction of 0.2 and $Re_m = 300$. As expected the resolution required for a numerically converged result is higher compared to that required for $Re_m = 40$ at the same volume fraction of 0.2.

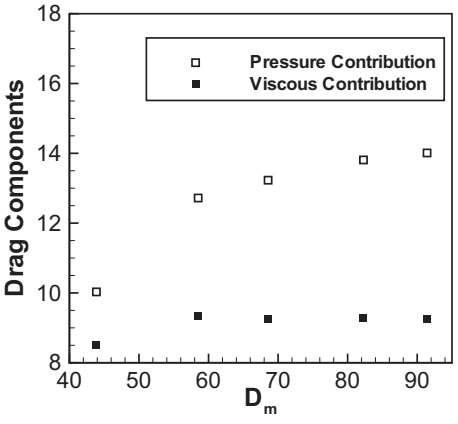

Fig. 4. Convergence characteristics of drag force due to fluctuating pressure (open symbols) and viscous stresses (filled symbols) for FCC arrays at $Re_m = 300$ with grid resolution D_m. Volume fraction ϕ is equal to 0.2.

For random arrays, in addition to errors arising from finite grid resolution, there is statistical variability between different realizations and the box length is an independent numerical parameter. The choice of L/D is determined by two requirements: (i) spatial autocorrelation of velocity should decay within the box length and (ii) there should be sufficient number of particles in the box for a statistically reliable estimate of the average normalized force.

An initial estimate for the minimum box length required can be found from the Brinkman screening length. Brinkman screening is the phenomenon whereby the fluid velocity disturbance produced by each particle is decreased due to the force exerted by the fluid on the neighboring particles. It plays a crucial role in limiting the range of fluid velocity correlations. The length scale l_b over which the fluid correlations decay is termed the Brinkman screening length (Hinch, 1977; Hill et al., 2001a) and it decreases with increasing volume fraction ($l_b \sim O(D/(2\sqrt{\phi}))$).

Decay of the fluid velocity autocorrelation $\rho_u(r)$ that is defined as

$$\rho_u(r) = \frac{\left\langle I_f(\mathbf{x})\mathbf{u}''^{(f)}(\mathbf{x}) \cdot I_f(\mathbf{x}+\mathbf{r})\mathbf{u}''^{(f)}(\mathbf{x}+\mathbf{r})\right\rangle}{\left\langle I_f \mathbf{u}''^{(f)} \cdot \mathbf{u}''^{(f)}\right\rangle}, \tag{36}$$

for steady flow past a random configuration of spheres ($\phi = 0.2$), is shown in Fig. 5 for two values of mean flow Reynolds numbers ($Re_m = 20$ and 300). Strictly speaking the fluid velocity autocorrelation is anisotropic, but the isotropic definition is used to obtain an estimate of the autocorrelation length. For both Reynolds numbers, the fluid velocity autocorrelation function decays to zero around $x = 0.2L$, while the estimate for Brinkman screening length is $0.15L$. Thus the Brinkman screening length can be used as a good estimate to determine the required box length. However, if we choose a box length that is comparable to or slightly greater than the Brinkman screening length, we get very few spheres in the box and this leads to high statistical variability in the drag force. The box lengths that we choose to perform the PUReIBM simulations are much larger than the Brinkman screening lengths and we have used values from past LBM simulations as a guideline.

In summary, these numerical convergence test results show that PUReIBM simulations yield grid-independent values for the mean drag. These results are also independent of the choice of time step used to advance the solution in pseudo time, provided the stability criterion is met. A satisfactory number of MIS should ideally be determined by determining the minimum number of samples for a given level of statistical error in the force estimate. However, this

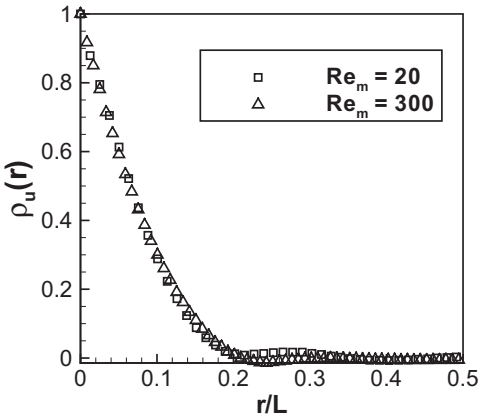

Fig. 5. Decay of the fluid velocity autocorrelation function obtained from PUReIBM simulation of steady flow past a random configuration of spheres at a solid volume fraction of 0.2 and mean flow Reynolds numbers 20 (squares) and 300 (triangles). In these simulations L/D ratios of 6 and 4.5 are used for Reynolds numbers 20 and 300 respectively.

quantity is a strong function of Re_m and solid volume fraction. To report estimates for the average normalized force for random arrays, we used 5 MIS at all volume fractions and Reynolds numbers. Clearly, the requirements of minimum L/D, minimum D_m, and minimum $\mathcal{M}$, together dictate a trade-off for a fixed level of computational work. Of these parameters, our tests reveal that the numerical error in PUReIBM exhibits the highest sensitivity to grid resolution D_m.

6. Numerical tests

PUReIBM has been validated by comparing the drag force obtained from simulations of flow past an isolated sphere with the single sphere drag correlation given by Schiller and Naumann (1935) (see Garg et al. (2011)). Since it is difficult to find an experimental data set to validate simulations of dense suspensions that use periodic boundary conditions, we compare our results with previous numerical or analytical works. We compare the drag force obtained from PUReIBM simulations for the following test cases:

1. Stokes flow past simple cubic (SC) and face centered cubic (FCC) arrangements (ranging from dilute to close-packed limit) with the boundary-integral method of Zick and Homsy (1982).
2. Stokes flow past random arrays of monodisperse spheres with LBM simulations of van der Hoef et al. (2005).
3. moderate to high Reynolds ($Re_m \leqslant 300$) in SC and FCC arrangements with LBM simulations of Hill et al. (2001b).
4. flow past random arrays of monodisperse spheres at $Re_m = 100$ with ANSYS-FLUENT CFD package (see Section 8.1).

6.1. Stokes flow

We first consider Stokes flow past ordered and random arrays of equisized spheres. Different analytical and numerical techniques, such as analytical solution to the Stokes equations (Hasimoto, 1959), Galerkin methods (Snyder and Stewart, 1966; Sorensen and Stewart, 1974), and the boundary-integral method (Zick and Homsy, 1982) have been used to determine the drag force in Stokes flow past ordered arrays as a function of solid volume fraction. Since Zick and Homsy's results are within 6% of all the other studies, and include all three ordered configurations for the entire range of solid volume fraction, their results are used as a benchmark to compare with PUReIBM simulations. Fig. 6a shows that the PUReIBM simulations are in excellent agreement with reported values from dilute to close-packed limits. Moreover, PUReIBM is able to capture the slightly different dependence of $F(\phi)$ for SC (as compared to FCC) for $\phi > 0.3$. The grid resolution in the PUReIBM simulations for the FCC cases is 25.24 and 104 grid points per particle diameter, for the minimum and maximum volume fractions of 0.01 and 0.698 considered, respectively. In the simple cubic cases, D_m is equal to 40.08 and 149, for the minimum and maximum volume fractions of 0.01 and 0.514, respectively.

Stokes flow past random arrays of spheres has been studied extensively by several researchers(Hill et al., 2001a; van der Hoef et al., 2005). In Fig. 6b we compare the Stokes drag obtained from PUReIBM simulations of flow past random arrays of monodisperse spheres with the drag correlation of van der Hoef et al. (2005). From this figure we can see that the results from PUReIBM simulations are in excellent agreement with the LBM-based correlation for Stokes drag in random arrays.

6.2. Moderate reynolds numbers

Hill et al. (2001b) performed an extensive study of flow past ordered SC and FCC arrangements at moderate Reynolds numbers using LBM simulations. We compare the drag values for moderate

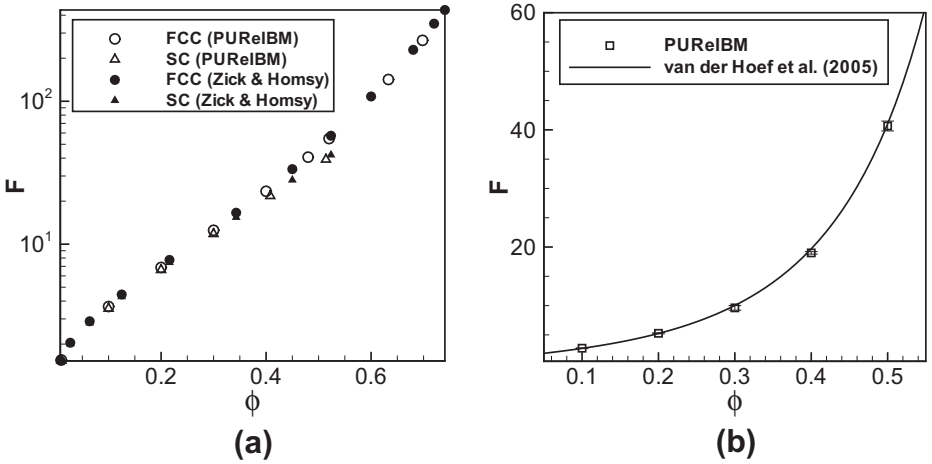

Fig. 6. Variation of the normalized drag force as a function of the solid volume fraction ϕ in Stokes flow past SC, FCC and random arrangements of spheres. In (a) drag values obtained from PUReIBM simulations (open symbols) of Stokes flow in SC and FCC arrangements are compared with the results Zick and Homsy (1982) (filled symbols). In (b) drag values from PUReIBM simulations of Stokes flow in random arrays of spheres are compared with the Stokes drag correlation proposed by van der Hoef et al. (2005). For each volume fraction the normalized force from PUReIBM simulations is reported by averaging over 5 MIS and the error bars on the symbols in this figure represent 95% confidence intervals in the estimation of the normalized force.

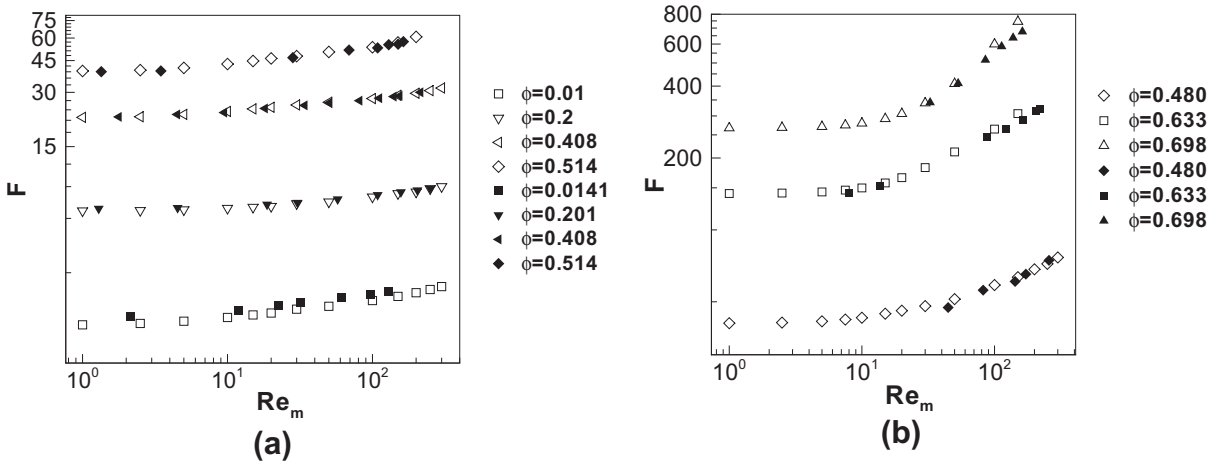

Fig. 7. Variation of the normalized drag force as a function of both the solid volume fraction and mean flow Reynolds number for flow past SC and FCC arrays. In all these cases, the mean flow is directed along the positive x–axis. In (a) drag obtained from PUReIBM simulations (open symbols) for SC arrangements is shown while in (b) drag obtained for FCC arrangement is shown. In both figures, PUReIBM drag values are compared with those reported by Hill et al. (2001b).

Reynolds number flow in SC and FCC arrangements obtained from PUReIBM simulations with those reported by Hill et al. (2001b) in Fig. 7a and b respectively. HKL note that the normalized drag force in ordered arrays is a strong function of the flow angle. To avoid additional parameterization of the problem by flow angle, the validation tests shown in this section are performed for the case where the mean flow is directed along the positive x-axis. These figures show that drag values for ordered arrays are in excellent agreement with those reported by Hill et al. (2001b).

The validation tests described in this section show that the PUReIBM simulations faithfully reproduce many standard results published in literature. Before we present the results for flow past random arrays of spheres at moderate Reynolds numbers, it is important to understand the rationale behind choosing the simulation setup that we used. It is also important to compare the simulation setup used in this work with those used by HKL, BVK (and several other) for similar studies.

7. Comparison of simulation setups to extract computational drag laws

To specify a closure for the interphase momentum transfer term, it is natural to simulate a statistically homogeneous suspension flow with freely moving particles and to then compute volume-averaged estimates of the average fluid–particle force from the particle acceleration data. Due to the large number of parameters encountered in gas–solid flow, it is advantageous to use a fixed bed setup so that the parameter space can be explored relatively easily. Another advantage of using fixed bed setups is that it is easy to design an experimental setup that mimics the simulation setup. Use of fixed bed simulation methodology to extract computational drag laws for gas–solid flows is justified if the configuration of the particles changes very slowly compared to the time it takes to attain mean momentum balance. The time scale over which the particle configuration changes depends on $\mathrm{Re}_T = DT^{1/2}/\nu_f$, which is the Reynolds number based on the particle fluctuating velocity that is characterized by the particle granular temperature T. The particle granular temperature T is a measure of the variance in the particle velocities and is defined as $T = 1/3\langle \mathbf{v}'' \cdot \mathbf{v}'' \rangle$, where $\mathbf{v}''$ is the fluctuation in the particle velocity defined with respect to the mean particle velocity. Particle-resolved simulations of freely evolving suspensions (Tenneti et al., 2010) and recent high-speed imaging of particles (Cocco et al., 2010) show that this value of Re_T is low for high Stokes number suspensions.

Although fixed bed simulations can be used to infer drag laws for gas–solids flow, care must be taken when extending this setup to simulate problems with non-zero Re_T and bi-disperse suspensions with relative velocity between both size classes. If all particles move with the same velocity (i.e., $\mathrm{Re}_T = 0$), a change of frame renders the fixed bed setup a Galilean-Invariant (GI) transformation of the physical problem. This is not the case for non-zero Re_T. Similarly for bi-disperse suspensions with non-zero relative velocity between size classes, a Galilean change of frame can bring only particles of one size class to rest, unless particles belonging to both size classes move with the same mean velocity.

The simulation setup used in this work is flow past infinitely massive particles initially at rest in a fluid ($\mathrm{Re}_T = 0$). Particle velocities do not change in time due to the infinite inertia of the particles and hence they remain at rest throughout the simulation. The desired mean flow Reynolds number (or flow rate) is specified and the mean pressure gradient required to produce the desired flow rate evolves in time to balance the force acting on the particles. We denote this setup A as described in Table 1.

The next simulation setup we consider is a GI equivalent of setup A, where the problem is solved in a frame moving with velocity equal to $\langle \mathbf{u}^{(f)} \rangle$ with respect to the laboratory frame. In this frame, the mean fluid velocity is zero and all the particles move with the same constant velocity of $-\langle \mathbf{u}^{(f)} \rangle$. In setup A′, if the equations of motion are written for a *fixed, non-deforming* control volume (CV), the positions of the particles must evolve in time due to the non-zero velocities of the particles. This setup A′ (cf. Table 1) is used by van der Hoef et al. (2005) and BVK to propose their respective drag laws.

Setup A′ can also be solved by considering a *moving, non-deforming* control volume that moves with the particle velocity $\mathbf{V}^{(p)}$ such that particle positions do not change with respect to the control volume (note that all the particles move with the same velocity, i.e., $\mathrm{Re}_T = 0$). We denote this approach as setup B (cf. Fig. 8). Although the control volume is moving in this setup, we

Table 1
Summary of various simulation setups.

Setup	Average fluid velocity	Particle velocity	Particle position	Control volume
A	$\langle \mathbf{u}^{(f)} \rangle$	0	Fixed	Fixed
A′	0	$-\langle \mathbf{u}^{(f)} \rangle$	Moving	Fixed
B	0	$-\langle \mathbf{u}^{(f)} \rangle$	Fixed	Moving
C(non GI)	0	$-\langle \mathbf{u}^{(f)} \rangle$	Fixed	Fixed

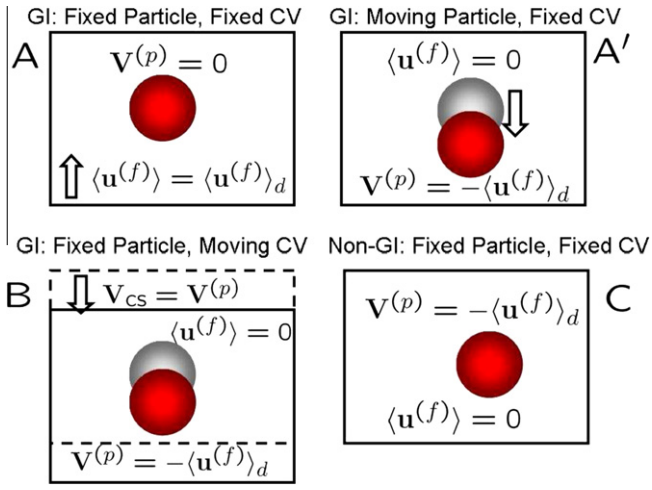

Fig. 8. Schematic comparing various simulation setups.

must remember that the solution fields and particle velocities are with respect to the frame of setup A′. For a moving control volume the convective flux is written with respect to the control volume and hence the nonlinear term in setup B is different from that in setup A or A′.

All the setups A, A′ (fixed CV) and B (moving CV) are GI transformations of the same physical problem and thus any computational method should yield the same solution when viewed in the appropriate reference frame. In particular, quantities such as the steady mean drag that are GI should be identically reproduced by any numerical method, irrespective of the chosen setup.

Besides the setups discussed above, a *non-Galilean-invariant* setup is sometimes used to solve the physical problem. In this setup denoted C (cf. Table 1), the particles are all assigned the same velocity, but their positions are fixed to their initial locations and the equations of motion are written for a *fixed, non-deformable* control volume. Since setup C is not a GI transformation of the physical problem it is an *incorrect* setup, although the error incurred in the limit of Stokes flow is negligible. In this section we show that we obtain GI solutions from PUReIBM simulations of setups A, A′ and B. We also show how the incorrect non-GI setup C leads to erroneous results at $Re_m = 150$.

We consider a simple cubic arrangement of spheres at a volume fraction of 0.4 and mean slip Reynolds number of 150. In Fig. 9, the steady state velocity field obtained from PUReIBM simulations for the different setups (A, A′, B and C) are compared. All these velocity fields are viewed in the reference frame of setup A (laboratory frame). From these figures we can see that while setups A, A′ and B give the same solution fields, the solution obtained from setup C is significantly different. So we expect that the drag force, which is obtained by integrating the pressure and viscous stress over the particle surface, will also be significantly different. Fig. 10 compares the evolution of the normalized pressure and viscous forces for all the setups. As expected, the evolution of both pressure and viscous contributions to the drag force in the incorrect non-GI setup C is significantly different from those obtained from other GI setups.

In particular, setups A and B are very useful to extract computational drag laws for fixed beds because the motion of the particles need not be considered. But this simplification is possible as long as all the particles are initialized with the same velocity. When the particles have different velocities there exists no

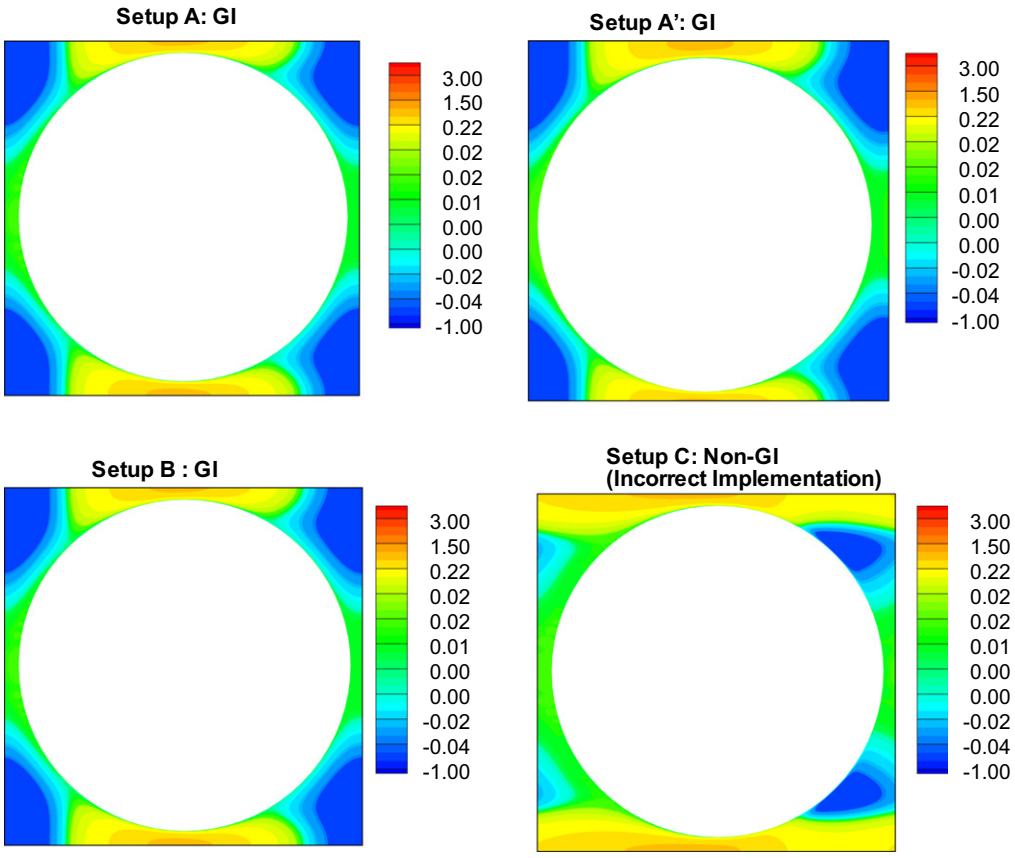

Fig. 9. Plot comparing the velocity contours obtained from the different simulation set ups. The contours shown in this figure are for a simple cubic arrangement at a volume fraction of 0.4 and mean flow Reynolds number of 150.

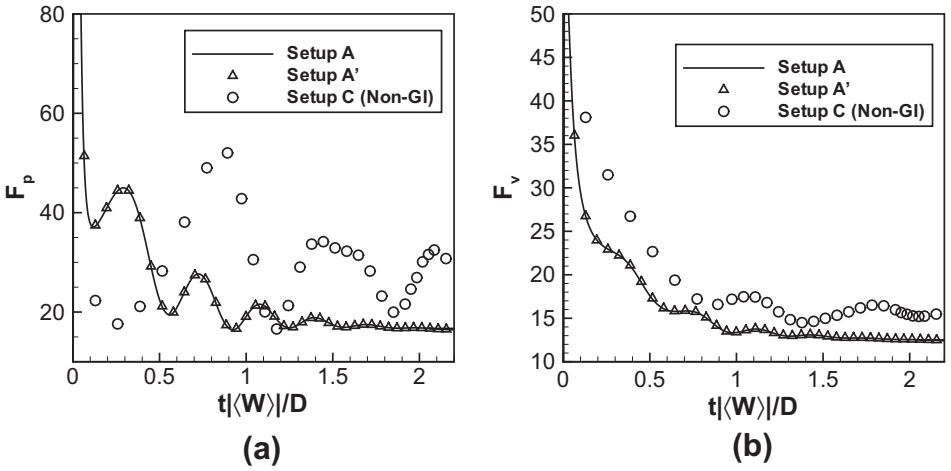

Fig. 10. Plot comparing the evolution of normalized pressure and viscous forces obtained from the different simulation setups shown in Fig. 8. The volume fraction is 0.4 and the mean flow Reynolds number is 150. Pressure force is plotted in (a) while the viscous force is plotted in (b). Since the results obtained from setups A, A′ and B are identical, only two (A and A′) are shown in these plots for clarity.

Galilean-invariant transformation such that all the particles appear fixed to their initial locations. Such problems can only be solved using setup A′. Recently Yin and Sundaresan (2009a,b) and Holloway et al. (2010) used setup C to propose LBM based drag correlations to account for the relative slip velocity between particles. The work of Yin and Sundaresan (2009a,b) is limited to the Stokes flow regime and hence the use of setup C is a valid approximation because the particles might not even move one grid cell during the simulation. However, the applicability of setup C to the higher Reynolds number simulations of Holloway et al. (2010) needs to be examined more closely. PUReIBM simulations of SC arrays using the non-GI setup C revealed that the the drag obtained from setup C is in reasonable agreement with the drag obtained from the other GI setups only up to a Reynolds number of 50, and differs substantially beyond that. This clearly shows that simulations of high Reynolds number flow past particles using a non-GI setup will lead to wrong results. Holloway et al. (2010) did not perform any simulations beyond Reynolds number of 50 and so their results are probably within 10% of the results obtained from other GI setups. We now present the results obtained from PUReIBM simulations of flow past random arrays of spheres at moderate Reynolds numbers using setup A.

8. Results

We performed PUReIBM simulations of flow past fixed random configurations of particles at Reynolds numbers up to 300 and for solid volume fractions in the range of 0.1–0.5. The numerical resolutions used in PUReIBM simulations are either comparable or higher than those used by HKL and BVK (cf. Table 2). Values of the normalized force obtained from PUReIBM simulations are compared with those reported by HKL and BVK in Fig. 11. Normalized force values for volume fractions 0.1, 0.2 and 0.3 are shown in Fig. 11a while force values for volume fractions 0.4 and 0.5 are shown in Fig. 11b. It can be seen that PUReIBM simulations are in good agreement with the data reported by HKL. The average percentage difference between PUReIBM and HKL drag values is about 8% while a maximum difference of 20% is observed at a volume fraction of 0.4 and a mean flow Reynolds number of 120. One reason for this discrepancy at $\phi = 0.4$ is that although HKL reported their results for a nominal volume fraction of 0.4, the actual volume fraction that they simulated was 0.410 (Hill et al., 2001b). At higher Reynolds numbers the change in the force due to change in volume fraction can be quite significant. For instance, at $Re_m = 100$, the normalized force obtained at a $\phi = 0.4$ is almost twice the normalized force obtained at $\phi = 0.3$.

Table 2
Comparison of the numerical parameters (number of particles N_p, number of MIS $\mathcal{M}$, particle diameter in grid units D_m and the ratio of the length of the box to the particle diameter L/D) used for random arrays in PUReIBM simulations with the past LBM simulations of HKL and BVK. For each entry, first and second rows correspond, respectively, to the LBM simulations of HKL and BVK, and the third row corresponds to the current PUReIBM simulations. For the PUReIBM simulations, different numerical parameters are used for $Re_m \leqslant 100$ and $Re_m > 100$. These are separated by "/". Numbers before the "/" correspond to $Re_m \leqslant 100$ while numbers after the "/" correspond to $Re_m > 100$. At volume fraction 0.5 PUReIBM simulations are performed only up to a Reynolds number of 100.

ϕ	N_p	$\mathcal{M}$	D_m	L/D
0.1	16	5	9.6	4.38
	54	20	17.5	6.6
	80/41	5	20/30	7.5/6
0.2	16	5	17.6	3.47
	54	20	17.5	5.2
	161/34	5	20/40	7.5/4.5
0.3	16	5	17.6	3.06
	54	20	21.5	3.07
	71/26	5	30/50	5/3.6
0.4	16	5	33.6	2.73
	54	20	21.5	4.13
	95/20	5	30/60	5/3
0.5	16	5	33.6	2.56
	54	20	21.5	3.84
	61/–	5	40/–	4/–

We can see from Table 2 that the numerical resolution used by HKL and in PUReIBM simulations are comparable up to $Re_m = 100$. The grid resolutions reported for HKL in Table 2 are those used for the highest Reynolds numbers that they simulated. HKL used much coarser meshes to simulate lower Reynolds numbers. For $Re_m > 100$ the PUReIBM simulations are performed with much higher resolutions and HKL did not perform any simulations for $Re_m > 100$ for most volume fractions. A comparison of the simulation data with the drag correlation proposed by HKL showed that beyond $Re_m = 100$, differences between the PUReIBM simulation data and the HKL drag correlation increased with increasing Re_m. Since HKL did not explore a wider range of Reynolds numbers, this work provides a more accurate variation of the normalized force with Reynolds number.

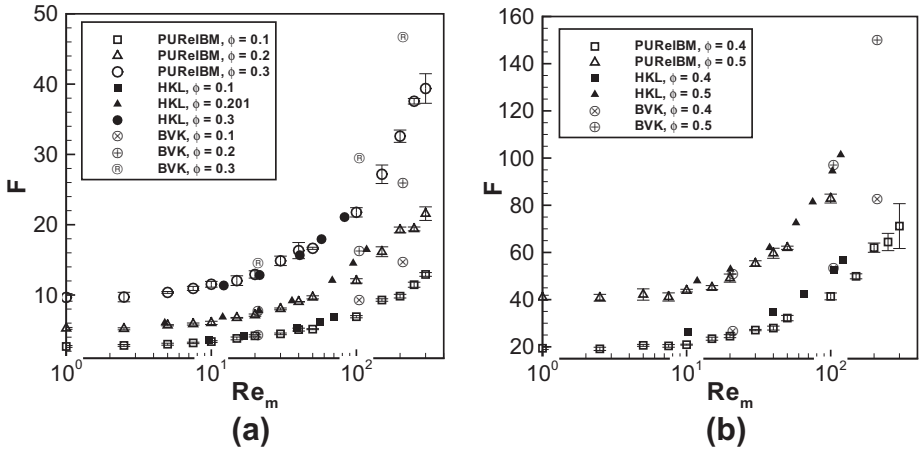

Fig. 11. Variation of normalized force with Reynolds number for random assembly of fixed particles. Drag values obtained from PUReIBM simulations (open symbols) are compared with those reported by HKL (filled symbols) and BVK. In left panel Fig. 7a $\phi = 0.1,0.2,0.3$ and in the right panel Fig. 7b $\phi = 0.4,0.5$.

From Fig. 11 we see that PUReIBM drag values differ substantially from those reported by BVK. A difference of about 30% is consistently observed at a Reynolds number of 200 for all volume fractions while a difference of 20% is observed at a Reynolds number of 100. BVK used a constant resolution of 17.5 lattice units across a particle diameter was for $\phi \leqslant 0.2$, and for higher volume fractions, their results were obtained by averaging the drag obtained using two different resolutions of 17.5 and 25.5 lattice units. Therefore, in Table 2, we have used the average value of 21.5 lattice units to report their resolutions for $\phi \geqslant 0.3$. At a given volume fraction, they used a constant grid resolution to simulate Reynolds numbers ranging from 21 to 1000. As the volume fraction increases, the number of grid/lattice nodes in the gaps between the spheres decrease and a progressively higher grid resolution is required. In the HKL study the particle resolution was increased from 9.6 lattice units per particle diameter for the lowest volume fraction of 0.1 to 41.6 lattice units for the highest volume fraction of 0.641, which is a four-fold increase. However, in the BVK study the particle resolution increased by only a fraction for a wide volume fraction range of 0.1–0.6. Table 2 shows that the PUReIBM simulations are consistently better resolved in terms of the number of particles, grid resolution, and the box-size. BVK performed greater number of MIS but the scatter in PUReIBM data does not point to a need for such high number of MIS. In addition to the numerical parameters, PUReIBM and BVK simulations differ in the simulation setup. While PUReIBM simulations are performed using setup A, the simulations of BVK are performed using setup A′.

We also studied the effect of using a non-GI setup to simulate flow past random arrays at higher Reynolds numbers. We performed PUReIBM simulations of flow past random arrays using the setup C for two different volume fractions (0.2 and 0.3). Fig. 12 shows the variation of the normalized fluid–particle force with Reynolds number obtained from setups A and C. It is interesting to note from this figure that the force obtained from setup C is in excellent agreement with the BVK drag correlation.

To summarize, PUReIBM simulations show an excellent match with the drag correlations proposed by HKL and BVK for low Reynolds number for both dilute and moderately dense random arrays. However, PUReIBM simulations show a significant departure from these correlations at higher Re_m. The drag law proposed by HKL is stated to be more reliable for all Reynolds numbers only at higher volume fraction. The BVK drag correlation is proposed based on a fit to the drag values obtained from simulating only 5 different Reynolds numbers between 20 and 1000. Their simulations are not as highly resolved as PUReIBM simulations and they might

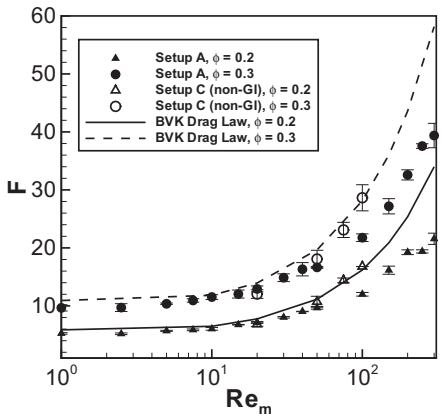

Fig. 12. Plot showing the variation of normalized fluid–particle force with Reynolds number for a random array at two different volume fractions ($\phi = 0.2,0.3$). Results obtained from both setups A and C are shown. The BVK drag correlation (lines) is also shown for comparison.

not be grid independent. Owing to the differences in the solution approach and numerical resolutions between PUReIBM and LBM based studies, an independent verification with a body-fitted solver is required to assess the accuracy of PUReIBM and LBM simulations of flow past fixed assemblies of randomly distributed particles with finite fluid inertia. In the following subsection we compare results from PUReIBM simulations with those obtained from a body-fitted grid.

8.1. Comparison of PUReIBM with body-fitted grid simulations

We assess the accuracy of PUReIBM simulations by comparing the results obtained from PUReIBM with those obtained by solving the same problem using ANSYS-FLUENT, which uses a body-fitted solver. We simulated flow past the same random configuration using PUReIBM and ANSYS-FLUENT to directly compare pressure and velocity fields. This random configuration was taken from one of the 5 independent configurations that we simulated using PUReIBM at a volume fraction of 0.4 and mean flow Reynolds number of 100.

We performed a grid refinement study of the ANSYS-FLUENT solver by simulating flow past the chosen random configuration using four different resolutions. The coarsest mesh we used has

60,000 tetrahedral cells while the finest mesh has 3.25 million tetrahedral cells. We used a second-order upwind method for discretization of the convective terms. The simulation was stopped after the scaled residuals dropped by six orders of magnitude, and the drag acting on the suspension reached a steady state. In Fig. 13, we show the grid-convergence characteristics of the normalized force obtained from both ANSYS-FLUENT and PUReIBM simulations. Grid resolution of ANSYS-FLUENT is shown on the bottom x-axis while that of PUReIBM simulations (open triangles) is shown on the top. From the figure we conclude that the results obtained from PUReIBM and ANSYS-FLUENT simulations are numerically converged. Moreover, the grid-independent drag value obtained from the PUReIBM simulation on the finest mesh ($D_m = 40$) is within 1% of the grid independent drag value that is obtained from the ANSYS-FLUENT simulation. We also show the drag predicted by the LBM simulations of BVK (open circle) on this plot. Their simulations correspond to $D_m = 21.5$ and it is clear that the value predicted by the BVK drag law does not agree well with that predicted by PUReIBM or ANSYS-FLUENT. Since the drag law of BVK is obtained by averaging over 20 different particle configurations, this difference in drag cannot be attributed to the dependence on particle configurations.

We also compared the velocity and pressure fields obtained from PUReIBM and ANSYS-FLUENT simulations. Fig. 14 shows contours of the streamwise component of fluid velocity while Fig. 15 shows the contours of pressure on a cut-plane in the middle of the box. In this figure the flow is fom left to right. It is important to remember that PUReIBM uses a pseudo-spectral method on Cartesian grids while ANSYS-FLUENT uses a finite volume method on a body-fitted mesh. Given the differences between the differencing operators and the nature of interpolation errors in the two codes, the agreement obtained in Figs. 14 and 15 is excellent. Thus we conclude that PUReIBM computes solutions to the governing equations for gas–solids flow with an accuracy comparable to that of a body-fitted solver.

Since the drag in PUReIBM is computed from this flow solution by calculating stress at the particle surface, this gives confidence that the surface force density that is used to calculate the total drag is indeed accurately computed. Using PUReIBM we can look at the relative contribution of pressure and viscous terms to the total drag and also the local profiles of pressure and viscous drag forces.

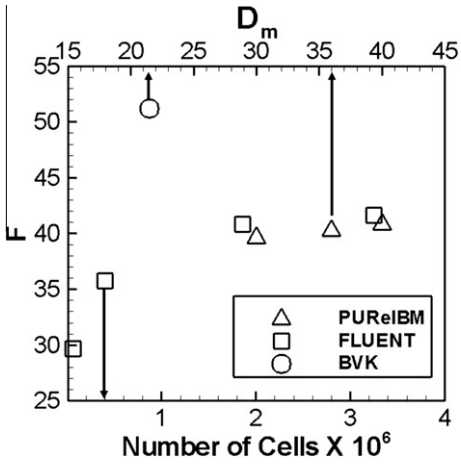

Fig. 13. Plots showing the grid convergence of ANSYS-FLUENT software and PUReIBM. Grid resolution of ANSYS-FLUENT (squares) corresponds to the bottom x-axis while the grid resolution of PUReIBM simulations (triangles) is shown in the top x-axis. The drag value reported by BVK at this volume fraction (0.4) and Reynolds number (100) is also shown for reference.

8.2. Relative contributions of pressure and viscous drag

At steady state, the mean pressure gradient is balanced by the pressure and viscous forces acting on all the particles such that

$$-(1-\phi)V\langle \mathbf{g}_{\mathrm{IBM}}\rangle_{\mathcal{V}} = -\oint_{\partial \mathcal{V}_s} \psi \mathbf{n}^{(s)} dA + \mu_f \oint_{\partial \mathcal{V}_s} (\nabla \mathbf{u}') \cdot \mathbf{n}^{(s)} dA, \tag{37}$$

where the total force acting on the suspension is $-\langle \mathbf{g}_{\mathrm{IBM}}\rangle_{\mathcal{V}} V$ and the ψ is the fluctuating pressure. The average force acting per particle, $\langle \mathbf{f}\rangle$, is obtained by dividing the total force by the total number of particles:

$$\langle \mathbf{f}\rangle = -\frac{1}{N_p}\langle \mathbf{g}_{\mathrm{IBM}}\rangle V.$$

Dividing Eq. (37) by N_p, the average force per particle is the sum of average pressure force per particle $\langle \mathbf{f}_p\rangle$ and average viscous force per particle $\langle \mathbf{f}_v\rangle$, i.e.,

$$(1-\phi)\langle \mathbf{f}\rangle = \langle \mathbf{f}_p\rangle + \langle \mathbf{f}_v\rangle. \tag{38}$$

While the vector Eq. (38) is always true, the following scalar equation for the normalized force $F(F = |\langle \mathbf{f}\rangle|/F_{\mathrm{Stokes}})$

$$(1-\phi)F(\phi, \mathrm{Re}_m) = F_p(\phi, \mathrm{Re}_m) + F_v(\phi, \mathrm{Re}_m), \tag{39}$$

holds only when the vectors $\langle \mathbf{f}_p\rangle$ and $\langle \mathbf{f}_v\rangle$ are collinear. Here F_p and F_v are the magnitudes of the average pressure and viscous forces per particle normalized by F_{Stokes}. We verified that the pressure and viscous forces are collinear over a wide range of volume fraction and Reynolds numbers, and hence the sum of the normalized pressure and viscous forces gives the total normalized force.

The scaling of normalized pressure and viscous forces with mean flow Reynolds number gives insight into the powers of Re_m that should be used in the drag law for the total force. Simple scaling arguments dictate that the pressure force $|\langle \mathbf{f}_p\rangle| \sim \rho_f U_{\mathrm{slip}}^2 D^2$ and the viscous force $|\langle \mathbf{f}_v\rangle| \sim \mu_f U_{\mathrm{slip}} D$. Normalizing the magnitudes of pressure and viscous forces by F_{Stokes}, it is easy to see that the normalized pressure force varies linearly with Reynolds number and the normalized viscous force is independent of the Reynolds number. So taking $F_p \sim \mathrm{Re}_m$ and F_v independent of Re_m led HKL to propose the following form of the drag law at moderate Reynolds numbers:

$$F(\phi, \mathrm{Re}_m) = F_2(\phi) + F_3(\phi)\mathrm{Re}_m, \tag{40}$$

where $F_2(\phi)$ represents F_v and $F_3(\phi)$ represents the volume fraction dependence of F_p. HKL assumed that the viscous contribution to the drag force remains constant for all Reynolds numbers, but this was not verified from simulations. However, as Fig. 16 shows, the viscous drag is not independent of the Reynolds number, but it is a sublinear power of the mean flow Reynolds number. Fig. 16 confirms the assumption of HKL that the pressure drag is approximately linear for larger Reynolds numbers ($\mathrm{Re}_m > 40$).

From PUReIBM simulations we observe that at any given Reynolds number, the ratio F_p/F_v increases with increasing volume fraction. At a given volume fraction, F_p/F_v increases with Reynolds number as expected. However, the viscous contribution does not become negligible compared to pressure drag. In fact, for volume fractions 0.1 and 0.2 the ratio F_p/F_v exceeds 1 only when Re_m >100. We also observed that the Reynolds number at which the pressure drag exceeds the viscous drag decreases with increasing volume fraction.

8.3. Local profiles of pressure and viscous contributions to the fluid–particle drag force

Profiles of the local pressure and viscous drag can provide insight into the behavior of the pressure and viscous drag with varying mean flow Reynolds numbers and volume fractions. We

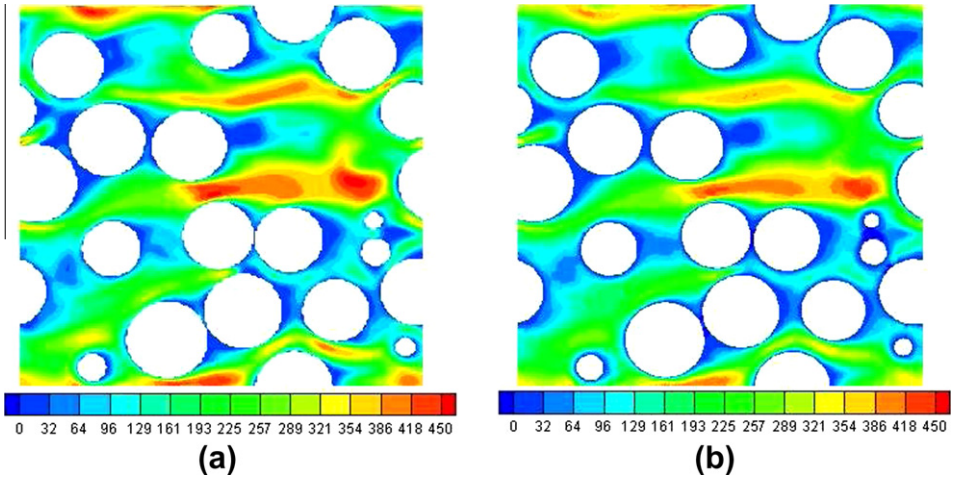

Fig. 14. Plots comparing the contours of the streamwise component of instantaneous fluid velocity obtained from PUReIBM (a) with those obtained from ANSYS-FLUENT software (b).

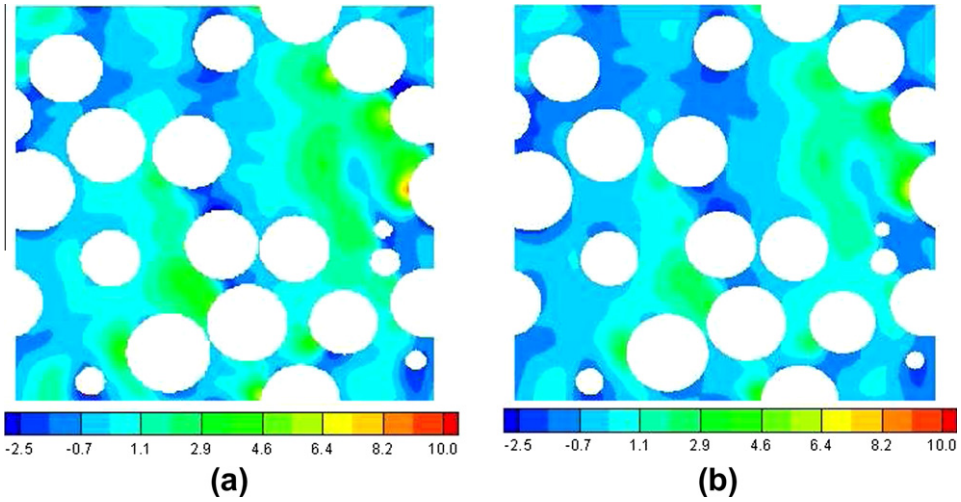

Fig. 15. Plots comparing the contours of instantaneous pressure obtained from PUReIBM (a) with those obtained from ANSYS-FLUENT software (b).

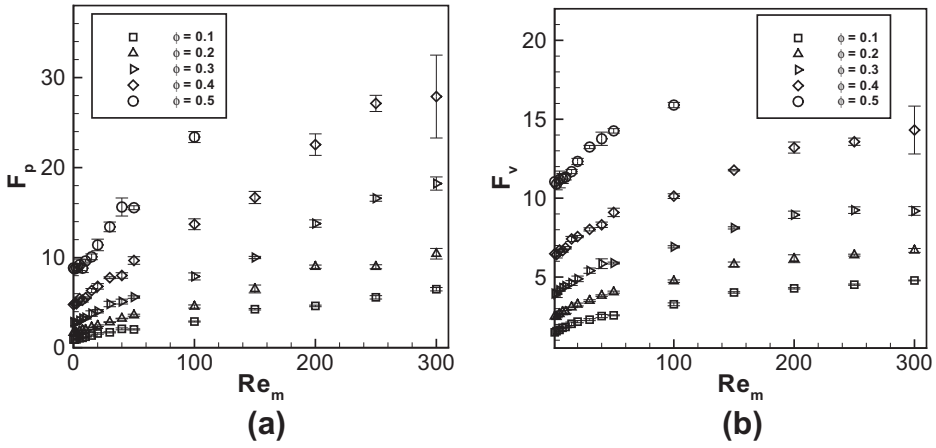

Fig. 16. Plots showing the pressure and viscous drag force in a random configuration.

examine the local profiles of pressure and viscous forces to facilitate the development of a drag law and to see if any self-similar scaling would emerge.

We define the local pressure and viscous contributions to the drag force with respect to the spherical coordinate system shown in Fig. 17. It is useful to define a unit vector $\mathbf{e}_{\parallel} = \langle \mathbf{W} \rangle / |\langle \mathbf{W} \rangle|$ along

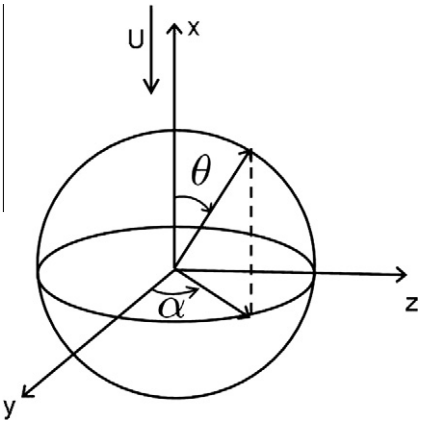

Fig. 17. Schematic of the spherical coordinate system used to define the local pressure and viscous drags. The polar angle in our convention is θ ($0 \leqslant \theta \leqslant \pi$) and the azimuthal angle is α ($0 \leqslant \alpha \leqslant 2\pi$).

the mean slip direction. In this work since the mean slip velocity is along the direction of the mean velocity of the fluid, we refer to the direction of the mean slip velocity as the streamwise direction. We examine the profiles of the streamwise components of the average pressure and viscous forces per particle along the polar angle. For every particle in the μth realization, the variation of the streamwise component of pressure and viscous forces along the polar angle is computed by averaging out the dependence on the azimuthal angle. The variations of average pressure and viscous forces per particle along the polar angle are then computed by averaging the local profiles over all the particles. The streamwise components of the average pressure and viscous forces per particle in the μth realization can be expressed as:

$$F^{\mathrm{loc}}_{p,\mu}(\theta) = \frac{1}{N_p}\sum_{n=1}^{N_p}\left(\int_0^{2\pi} -\psi(\theta,\alpha)\mathbf{n}^{(n)}\cdot\mathbf{e}_{\parallel}\,d\alpha\right)4\pi R^2,$$
$$F^{\mathrm{loc}}_{v,\mu}(\theta) = \frac{\mu_f}{N_p}\sum_{n=1}^{N_p}\left(\int_0^{2\pi} (\nabla\mathbf{u}'(\theta,\alpha)\cdot\mathbf{n}^{(n)})\cdot\mathbf{e}_{\parallel}\,d\alpha\right)4\pi R^2. \quad (41)$$

In the above equations, $\mathbf{n}^{(n)}$ is the unit normal vector pointing outward from the surface of the nth particle and $R = D/2$ is the radius of the particle. An ensemble-averaged estimate for the local pressure (F^{loc}_p) and viscous (F^{loc}_v) forces is then defined similar to Eq. (34). In Fig. 18 we plot the local coefficient of pressure $C^{\mathrm{loc}}_p(\theta)$ and the local skin friction coefficient $C^{\mathrm{loc}}_f(\theta)$ along the polar angle for different volume fractions and mean flow Reynolds numbers. The definitions of local coefficient of pressure and the local skin friction coefficient are similar to those used for a single sphere in an unbounded medium:

$$C^{\mathrm{loc}}_p(\theta) = \frac{F^{\mathrm{loc}}_p(\theta)}{\frac{1}{2}\rho_f\pi R^2((1-\phi)|\langle\mathbf{W}\rangle|)^2},$$
$$C^{\mathrm{loc}}_f(\theta) = \frac{F^{\mathrm{loc}}_v(\theta)}{3\pi\mu_f D(1-\phi)|\langle\mathbf{W}\rangle|}. \quad (42)$$

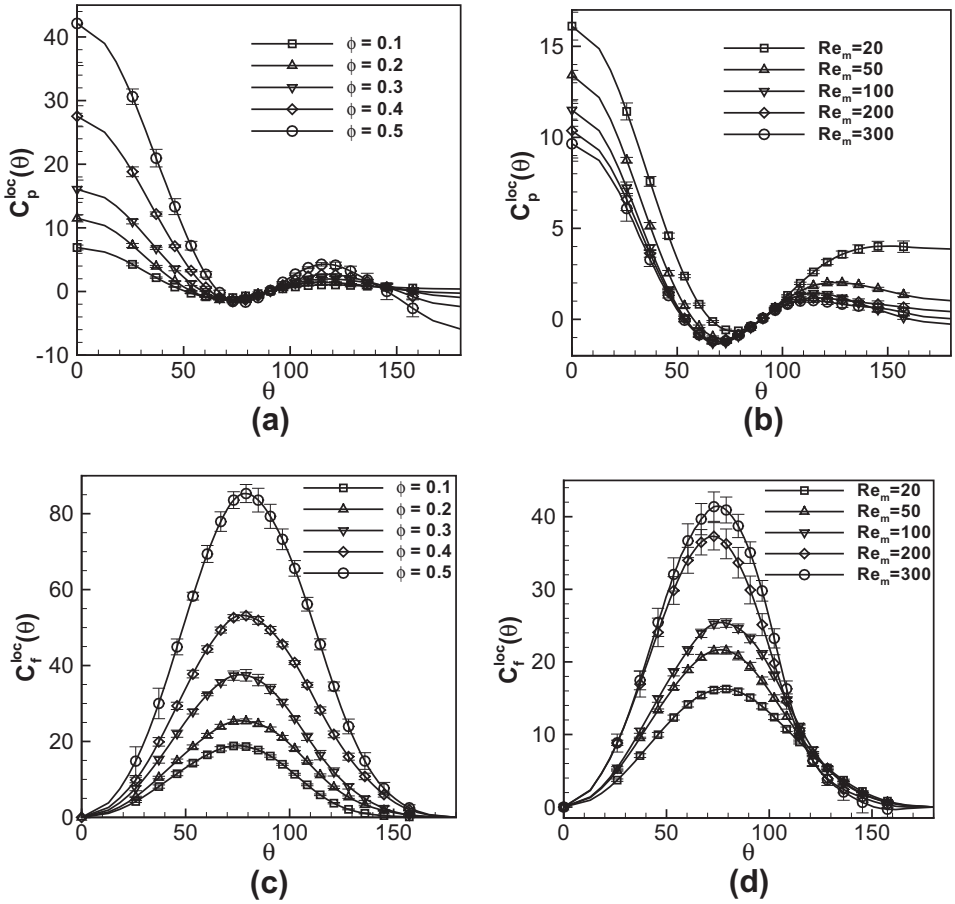

Fig. 18. Profiles of local coefficient of pressure and coefficient of friction along the polar angle. (a) shows the local pressure profiles for different volume fractions at a Reynolds number of 100 while (b) shows the local pressure profiles for various mean flow Reynolds numbers at a volume fraction of 0.2. Similarly (c) shows the local viscous drag profiles for different volume fractions at a Reynolds number of 100 while (d) shows the local viscous drag profiles for various mean flow Reynolds numbers at a volume fraction of 0.2.

The local profiles of pressure drag for different volume fractions at a mean flow Reynolds number of 100 are shown in Fig. 18a. Although there appears to be a local minimum at $\theta = 75^\circ$ for all the volume fractions we can see that there is no evident self-similarity in these profiles. The behavior of the local pressure profiles at the "trailing edge" is different for different volume fractions. In Fig. 18c we plot the local skin friction coefficient for different volume fractions at a Reynolds number of 100. The maxima of the viscous forces are found at locations where the pressure forces attain their minima.

In Fig. 18b we show the local pressure profiles for different mean flow Reynolds numbers at a volume fraction of 0.2 while the skin friction coefficients are plotted in Fig. 18d. We can see that at $\mathrm{Re}_m = 20$ the pressure drag nearly follows a sinusoidal profile up to an angle of 110° and remains approximately constant beyond this angle. This behavior is similar to that observed for a single sphere in an unbounded fluid, where the pressure nearly obeys the potential flow solution up to the point of separation and remains constant beyond this point. Also, at this volume fraction, for $\mathrm{Re}_m > 100$ the profiles of C_p^{loc} nearly collapse onto a single curve again verifying the assumption that the pressure force is quadratic in mean slip velocity.

The local profiles of pressure and viscous forces in random assemblies can be viewed as departures from those observed for an isolated sphere in an unbounded medium. These observations point to the fact that the drag law for random assemblies should be in the form of corrections to the single sphere drag law that reflect the dependence on ϕ and Re_m. It is clear that there is no obvious self-similarity that collapses the local pressure and viscous drag profiles as simple functions of volume fraction and Reynolds number.

9. A new correlation for the average fluid–particle drag

Based on the normalized force values obtained from PUReIBM simulations, the following function fits the data well with an average deviation of 2.5%:

$$F(\phi, \mathrm{Re}_m) = \frac{F_{\mathrm{isol}}(\mathrm{Re}_m)}{(1-\phi)^3} + F_\phi(\phi) + F_{\phi,\mathrm{Re}_m}(\phi, \mathrm{Re}_m). \tag{43}$$

Here, F_{isol} is the drag force acting on an isolated sphere moving in an unbounded medium. We used the single sphere drag correlation proposed by Schiller and Naumann (1935) to get the drag on an isolated sphere. The remaining two terms in (43) are given by

$$F_\phi(\phi) = \frac{5.81\phi}{(1-\phi)^3} + 0.48\frac{\phi^{1/3}}{(1-\phi)^4},$$

$$F_{\phi,\mathrm{Re}_m}(\phi, \mathrm{Re}_m) = \phi^3 \mathrm{Re}_m \left(0.95 + \frac{0.61\phi^3}{(1-\phi)^2}\right).$$

Fig. 19 compares the PUReIBM drag law given by (43) with existing drag correlations. We used the drag correlations of HKL, BVK, Gidaspow (1986) and Syamlal and O'Brien (1987) (referred to as S& B in Fig. 19) for comparison. The drag values computed from PUReIBM and HKL drag laws agree well upto $\mathrm{Re}_m = 100$. By

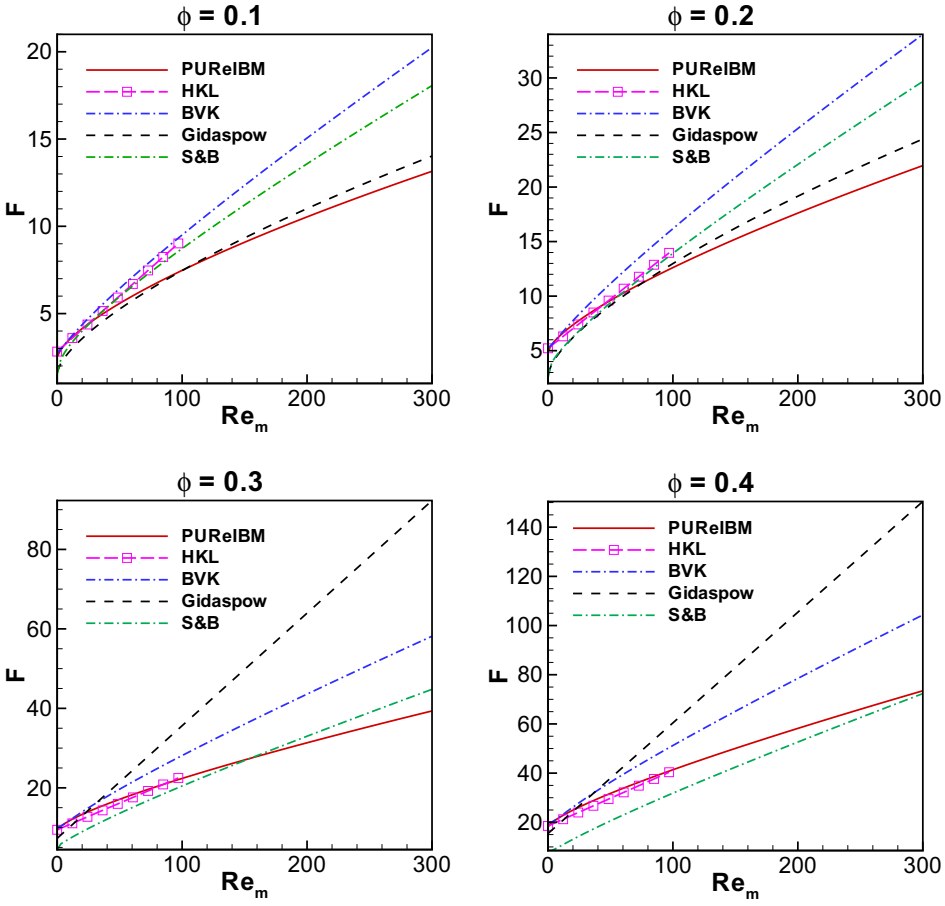

Fig. 19. Plot comparing the normalized force values obtained from the PUReIBM drag law (cf. (43)) with those obtained from the drag laws of HKL, BVK, Gidaspow (1986) and Syamlal and O'Brien (1987) for four different solid volume fractions. The volume fraction at which the drag values are computed is shown at the top of each panel. For every volume fraction, the HKL drag law terminates at $\mathrm{Re}_m = 100$ since it is not valid beyond that Reynolds number.

extending the HKL drag correlation beyond $Re_m = 100$, we noticed that the differences between PUReIBM and HKL drag law increase with Reynolds number. However, since HKL drag correlation is valid only upto $Re_m = 100$, comparison is not made beyond this Reynolds number. Differences between the BVK and PUReIBM drag law are more pronounced and increase significantly with increasing Reynolds number. At the largest Reynolds number that we simulated ($Re_m = 300$), PUReIBM and BVK drag laws differ by about 38%. This difference is observed consistently at all volume fractions. The power law dependence of drag on Reynolds number predicted by each of these drag laws is also different.

Also shown in Fig. 19 is the comparison between PUReIBM and the drag correlations of Gidaspow (1986) and Syamlal and O'Brien (1987), which are widely used in CFD simulations of gas–solid flow. Gidaspow's drag law reduces to the Wen–Yu drag law (Wen and Yu, 1966) when the solid volume fraction is less than 0.2 and for volume fractions greater than 0.2 it reduces to the Ergun equation (Ergun, 1952). Syamlal and O'Brien (1987) derived their drag law by converting terminal velocity correlations (Richardson and Zaki, 1954) to drag correlations. The behavior of these two drag laws with volume fraction and Reynolds number is very different from that of the PUReIBM drag law. We estimate that numerical error and statistical variability due to finite number of configurations contribute to an uncertainty of about 5% in the estimate of mean drag from PUReIBM simulations. So we conclude that differences of more than 30% observed in the values of drag obtained from PUReIBM and the BVK drag law are significant and can play an important role in the predictive capability of two-fluid model.

10. Summary

In this work we studied the steady drag in gas–solid flow with finite fluid inertia using particle-resolved DNS of flow past fixed monodisperse particle assemblies. We employ the Particle-resolved Uncontaminated-fluid Reconcilable Immersed Boundary Method (PUReIBM) to perform particle-resolved DNS of flow past fixed particle assemblies. In PUReIBM, the continuum Navier-Stokes equations with no-slip and no-penetration boundary conditions on each particle's surface are solved using an immersed boundary (IB) forcing term that is added to the momentum equation. The IB forcing in PUReIBM is solely restricted to those grid points that lie in the solid phase, and therefore the flow solution in the fluid phase is uncontaminated i.e., the unmodified Navier–Stokes equations are solved in the fluid phase. Through a comprehensive suite of tests it is demonstrated that PUReIBM is an accurate and numerically convergent particle-resolved DNS approach. We compared PUReIBM for flow past fixed particles at solid volume fraction of 0.4 and mean flow Reynolds number of 100 with ANSYS-FLUENT, which uses a body-fitted solver. We observed that the difference in the value of drag obtained from both methods is about 1%, and we obtained an excellent match of the velocity and pressure fields. Thus we conclude that PUReIBM computes solutions to the governing equations for gas–solid flow with accuracy comparable to that of a body-fitted solver.

The normalized force values obtained from PUReIBM agree reasonably well with the HKL drag law over a fairly wide range of volume fractions and mean flow Reynolds numbers. PUReIBM drag values differ by about 25% from the HKL drag law and by 38% from the BVK drag law at the largest Reynolds number that we simulated ($Re_m = 300$), and this difference is observed consistently at all volume fractions. Our simulations reveal a weak power-law dependence of the normalized viscous force on Re_m, reaching an asymptote at $Re_m > 200$ for all volume fractions. This replaces the prevailing notion that the normalized viscous force is independent of Re_m (Hill et al., 2001b). For the normalized pressure force , we concur with HKL that at moderate Reynolds numbers, the normalized pressure force can be approximated by a linear function in Re_m.

A new drag law for monodisperse suspensions is proposed using PUReIBM simulations of flow past fixed particle assemblies. Since this drag law is inferred from fixed particle assemblies, the effect of the mobility of particles is not captured in the drag correlation. However, the fixed bed approximation is valid for high Stokes number particles that are characteristic of gas–solid flows. The differences between the PUReIBM drag law and BVK drag law are more than 30% for $Re_m > 200$. The drag law is used to model the unclosed average interphase momentum transfer term in the mean momentum conservation equation of the two-fluid theory and determines the overall mean gas–solids flow structure. This improved PUReIBM drag law can enhance the predictive capability of CFD simulations of gas-solids flow that are based on the two-fluid theory. The improved drag law can also be used to refine the stability limits for gas–solid suspensions since these limits are determined by the functional dependence of drag on volume fraction.

Acknowledgements

This work is supported by Department of Energy Grant DE-FC26-07NT43098 through the National Energy Technology Laboratory (NETL). We would like to thank Mr. Bo Sun for his help with the calculation of the fluid-phase velocity autocorrelation function.

Appendix A. Derivation of mean momentum balance in the fluid-phase from the governing equations solved in PUReIBM

The derivation of mean momentum balance in the fluid-phase begins by volume-averaging the PUReIBM momentum conservation Eq. (19) over the fluid-phase region. Before proceeding with the volume-averaging, a simple expression is derived for the fluid-phase volume average of the gradient of any vector field. Consider any vector field $\mathbf{A}(\mathbf{x},t)$ that can be expressed as a gradient of some scalar field $Q(\mathbf{x},t)$, i.e. $\mathbf{A}(\mathbf{x},t) = \nabla Q$. The volume average of $\mathbf{A}(\mathbf{x},t)$ over the fluid-phase volume can be decomposed as the volume average over the entire domain $\mathcal{V}$ minus the volume average over the solid-phase $\mathcal{V}_s$ as

$$\int_{\mathcal{V}_f} \nabla Q(\mathbf{x},t)\mathbf{dx} = \int_{\mathcal{V}} \nabla Q(\mathbf{x},t)\mathbf{dx} - \int_{\mathcal{V}_s} \nabla Q(\mathbf{x},t)d\mathbf{x} + \mathbf{R}, \tag{A.1}$$

where $\mathbf{R}$ is the remainder term that accounts for the jump in Q at the particle–fluid interface, and $d\mathbf{x}$ is an infinitesimal volume. For a continuous Q field, there is no jump across the interface and the remainder term will be zero. However, in multiphase flows the shear and normal stresses are discontinuous across the interface and, therefore, the jump condition as implied by $\mathbf{R}$ should be accounted for.[3] Using the Gauss divergence theorem and noting that $\partial\mathcal{V}_f = \partial\mathcal{V}_f^{ext} \cup \partial\mathcal{V}^{int}$ (see Fig. 1), the volume integral over the fluid-phase volume can also be written as

$$\begin{aligned}\int_{\mathcal{V}_f} \nabla Q(\mathbf{x},t)\mathbf{dx} &= \oint_{\partial\mathcal{V}_f} Q\mathbf{n}^{(f)}dA \\ &= \oint_{\partial\mathcal{V}_f^{ext}} Q\mathbf{n}^{(ext)}dA + \oint_{\partial\mathcal{V}^{int}} Q^{(f)}\mathbf{n}^{(f)}dA,\end{aligned} \tag{A.2}$$

where dA is an infinitesimal area, $\mathbf{n}^{(f)}$ is the normal vector pointing outward from the interior fluid surface into the solid, $\mathbf{n}^{(ext)}$ is the

[3] The forcing approach used in PUReIBM results in continuous stress tensors across the interface and there is no need to account for the jump condition by $\mathbf{R}$. However, we prefer to use a more general approach here that is consistent with other methods such as the immersed interface method (Lee and Leveque, 2003; Xu and Wang, 2006).

normal vector pointing outward from the computational domain. In (A.2), $Q^{(f)}$ refers to the value of the Q field on the fluid side of the particle–fluid interface. Since the Q field is continuous along the computational domain $\partial\mathcal{V}$ (due to periodic boundary conditions), there is no need to specify Q as $Q^{(f)}$ in the first term.

The volume integral of $\nabla Q(\mathbf{x},t)$ over the solid-phase volume can be similarly written as

$$\int_{\mathcal{V}_s} \nabla Q(\mathbf{x},t)d\mathbf{x} = \oint_{\partial\mathcal{V}_s} Q\mathbf{n}^{(s)}dA = \oint_{\partial\mathcal{V}_s^{\text{ext}}} Q\mathbf{n}^{(ext)}dA + \oint_{\partial\mathcal{V}^{\text{int}}} Q^{(s)}\mathbf{n}^{(s)}dA, \tag{A.3}$$

where $\mathbf{n}^{(s)} = -\mathbf{n}^{(f)}$ is the normal vector pointing outward from the interior solid surface into the fluid. Substituting the above Eqs. (A.2) and (A.3) into (A.1), and noting that $\partial\mathcal{V} = \mathcal{V}_s^{\text{ext}} \cup \mathcal{V}_f^{\text{ext}}$ (Fig. 1), the remainder term $\mathbf{R}$ becomes

$$\mathbf{R} = \oint_{\partial\mathcal{V}^{\text{int}}} \left(Q^{(f)} - Q^{(s)}\right)\mathbf{n}^{(f)}dA. \tag{A.4}$$

With the above derivation of remainder term, we turn back our attention to the derivation of $\langle \mathbf{g}_{\text{IBM}}\rangle_{\mathcal{V}}$. Decomposing the pressure gradient term as $\mathbf{g}_{\text{IBM}} = \langle \mathbf{g}_{\text{IBM}}\rangle_{\mathcal{V}} + \nabla\psi$, the right hand side of the momentum conservation Eq. (19) can be written as

$$\frac{\partial \tau_{ji}^{\text{IBM}}}{\partial x_j} = -\langle g_{\text{IBM},i}\rangle_{\mathcal{V}} - \frac{\partial\psi}{\partial x_j} + \mu_f\frac{\partial^2 u_i'}{\partial x_j\partial x_j} + f_{u,i} = -\langle g_{\text{IBM},i}\rangle_{\mathcal{V}} + \frac{\partial\tau_{ji}}{\partial x_j} + f_{u,i}, \tag{A.5}$$

where the velocity field has been expanded using (21).

Integrating the momentum conservation Eq. (19) over the fluid-phase volume $\mathcal{V}_f$ and using (A.5) results in

$$\rho_f V_f \frac{d\left\langle u_i^{(f)}\right\rangle_{\mathcal{V}}}{dt} = -\langle g_{\text{IBM},i}\rangle V_f + \int_{\mathcal{V}_f}\frac{\partial\tau_{ji}}{\partial x_j}d\mathbf{x}. \tag{A.6}$$

In the above expression the volume average of the convective term is zero due to periodic boundary condition along $\partial\mathcal{V}_f^{\text{ext}}$ and zero penetration boundary condition on the fluid–particle interface $\partial\mathcal{V}^{\text{int}}$. Since the immersed boundary force is zero in the fluid-phase, its volume average over $\mathcal{V}_f$ is also zero. If the IB forcing is calculated at the particle–fluid interface and spread to the neighboring grid nodes that could lie in the fluid-phase, then the volume average of IB forcing $\left\langle \mathbf{f}_u^{(f)}\right\rangle_{\mathcal{V}_f}$ over $\mathcal{V}_f$ will be non-zero. As a result of this contamination of the fluid pressure and velocity fields by the IB forcing, the simulations will not exactly solve for the physical system that we wish to simulate.

Using (A.1) and the definition of $\mathbf{R}$ from (A.4), the volume-averaged momentum Eq. (A.6) becomes

$$\rho_f V_f \frac{d\left\langle u_i^{(f)}\right\rangle_{\mathcal{V}}}{dt} = -\langle g_{\text{IBM},i}\rangle_{\mathcal{V}} V_f + \int_{\mathcal{V}}\frac{\partial\tau_{ji}}{\partial x_j}\mathbf{dx} - \int_{\mathcal{V}_s}\frac{\partial\tau_{ji}}{\partial x_j}\mathbf{dx} + \oint_{\partial\mathcal{V}^{\text{int}}}\left(\tau_{ji}^{(f)} - \tau_{ji}^{(s)}\right)n_j^{(f)}dA. \tag{A.7}$$

The second term in the above equation is zero because the fluctuating stress tensor τ_{ji} is periodic along $\partial\mathcal{V}$. Using the decomposition in (A.3) for the third term in the above equation results in

$$\rho_f V_f \frac{d\left\langle u_i^{(f)}\right\rangle_{\mathcal{V}}}{dt} = -\langle g_{\text{IBM},i}\rangle_{\mathcal{V}} V_f - \oint_{\partial\mathcal{V}_s^{\text{ext}}}\tau_{ji}n_j^{(ext)}dA - \oint_{\partial\mathcal{V}^{\text{int}}}\tau_{ji}^{(s)}n_j^{(s)}dA + \oint_{\partial\mathcal{V}^{\text{int}}}\left(\tau_{ji}^{(s)} - \tau_{ji}^{(f)}\right)n_j^{(s)}dA, \tag{A.8}$$

where $\mathbf{n}^{(f)} = -\mathbf{n}^{(s)}$ has been substituted in the jump term. The surface integral of τ_{ji}' is zero along $\partial\mathcal{V}_s^{\text{ext}}$ due to periodicity. Noting the cancellation of two other terms, the above equation reduces to

$$\rho_f V_f \frac{d\left\langle u_i^{(f)}\right\rangle_{\mathcal{V}}}{dt} = -\langle g_{\text{IBM},i}\rangle_{\mathcal{V}} V_f - \oint_{\partial\mathcal{V}^{\text{int}}}\tau_{ji}^{(f)}n_j^{(s)}dA. \tag{A.9}$$

References

Abanades, J.C., Anthony, E.J., Lu, D.Y., Salvador, C., Alvarez, D., 2004. Capture of CO_2 from combustion gases in a fluidized bed of CaO. Environ. Energy Eng. 50, 1614–1622.

Anderson, T.B., Jackson, R., 1967. A fluid mechanical description of fluidized beds. Ind. Eng. Chem. Fundam. 6, 527–539.

Apte, S., Martin, M., Patankar, N., 2009. A numerical method for fully resolved simulation (FRS) of rigid particle flow interactions in complex flows. J. Comput. Phys. 228, 2712–2738.

Azar, C., Lindgren, K., Larson, E., Mollersten, K., 2006. Carbon capture and storage from fossil fuels and biomass – costs and potential role in stabilizing the atmosphere. Clim. Change 74, 47–79.

Bagchi, P., Balachandar, S., 2003. Effect of turbulence on the drag and lift of a particle. Phys. Fluids 15, 3496–3513.

Bagchi, P., Balachandar, S., 2004. Response of the wake of an isolated particle to an isotropic turbulent flow. J. Fluid Mech. 518, 95–123.

Beetstra, R., van der Hoef, M.A., Kuipers, J.A.M., 2007. Drag force of intermediate Reynolds number flows past mono- and bidisperse arrays of spheres. AIChE J. 53, 489–501.

Benyahia, S., Syamlal, M., O'Brien, T.J., 2005. Evaluation of boundary conditions used to model dilute, turbulent gas/solids flows in a pipe. Powder Technol. 156, 62–72.

Bokkers, G.A., Annaland, M.V.S., Kuipers, J.A.M., 2004. Mixing and segregation in a bidisperse gas–solid fluidised bed: a numerical and experimental study. Powder Technol. 140, 176–186.

Burton, T.M., Eaton, J.K., 2005. Fully resolved simulations of particle–turbulence interaction. J. Fluid Mech. 545, 67–111.

Carman, P.C., 1937. Fluid flow through granular beds. Trans. Inst. Chem. Eng. 15, 150–166.

Cocco, R., Shaffer, F., Hays, R., Reddy Karri, S.B., Knowlton, T., 2010. Particle clusters in and above fluidized beds. Powder Technol. 203, 3–11.

Cundall, P.A., Strack, O.D.L., 1979. A discrete numerical model for granular assemblies. Geotechnique 29, 47–65.

Drew, D.A., 1983. Mathematical modeling of two-phase flow. Annu. Rev. Fluid Mech. 15, 261–291.

Drew, D.A., Passman, S.L., 1998. Theory of Multicomponent Fluids. Springer.

Ergun, S., 1952. Fluid flow through packed columns. Chem. Eng. Prog. 48, 89–94.

Garg, R., 2009. Modeling and simulation of two-phase flows. PhD thesis, Iowa State University.

Garg, R., Galvin, J., Li, T., Pannala, S., 2010. Documentation of open-source MFIX-DEM software for gas–solids flows. Tech. Rep., National Energy Technology Laboratory, Department of Energy. <https://www.mfix.org>.

Garg, R., Tenneti, S., Mohd-Yusof, J., Subramaniam, S., 2011. Direct numerical simulation of gas–solids flow based on the immersed boundary method. In: Pannala, S., Syamlal, M., O'Brien, T.J. (Eds.), Computational Gas–Solids Flows and Reacting Systems: Theory, Methods and Practice. IGI Global, pp. 245–276.

Gidaspow, D., 1986. Hydrodynamics of fluidization and heat transfer: supercomputer modeling. Appl. Mech. Rev. 39, 1–23.

Ginzburg, I., d'Humières, D., 2003. Multireflection boundary conditions for lattice Boltzmann models. Phys. Rev. E 68, 066614.

Glowinski, R., Pan, T.W., Hesla, T.I., Joseph, D.D., Périaux, J., 2001. A fictitious domain approach to the direct numerical simulation of incompressible viscous flow past moving rigid bodies: application to particulate flow. J. Comput. Phys. 169, 363–426.

Hasimoto, H., 1959. On the periodic fundamental solutions of the Stokes equations and their application to viscous flow past a cubic array of spheres. J. Fluid Mech. 5, 317–328.

Hill, R.J., Koch, D.L., Ladd, A.J.C., 2001a. The first effects of fluid inertia on flows in ordered and random arrays of spheres. J. Fluid Mech. 448, 213–241.

Hill, R.J., Koch, D.L., Ladd, A.J.C., 2001b. Moderate-Reynolds-number flows in ordered and random arrays of spheres. J. Fluid Mech. 448, 243–278.

Hinch, E.J., 1977. An averaged-equation approach to particle interactions in a fluid suspension. J. Fluid Mech. 83, 695–720.

Holloway, W., Yin, X., Sundaresan, S., 2010. Fluid–particle drag in inertial polydisperse gas–solid suspensions. AIChE J. 56, 1995–2004.

Hu, H.H., Patankar, N.A., Zhu, M.Y., 2001. Direct numerical simulations of fluid-solid systems using the arbitrary Lagrangian–Eulerian technique. J. Comput. Phys. 169, 427–462.

Kashiwa, B., Gaffney, E., 2003. Design basis for CFDLib. Tech. Rep. LA-UR-03-1295, Los Alamos National Lab.

Kim, D., Choi, H., 2006. Immersed boundary method for flow around an arbitrarily moving body. J. Comput. Phys. 21, 662–680.

Kim, J., Moin, P., 1985. Application of a fractional-step method to incompressible Navier–Stokes equations. J. Comput. Phys. 59, 308–323.

Koch, D.L., 1990. Kinetic theory for a monodisperse gas–solid suspension. Phys. Fluids A 2, 1711–1723.
Koch, D.L., Sangani, A.S., 1999. Particle pressure and marginal stability limits for a homogeneous monodisperse gas-fluidized bed: kinetic theory and numerical simulations. J. Fluid Mech. 400, 229–263.
Ladd, A.J.C., 1994a. Numerical simulations of particulate suspensions via a discretized Boltzmann-equation. 1. Theoretical foundation. J. Fluid Mech. 271, 285–309.
Ladd, A.J.C., 1994b. Numerical simulations of particulate suspensions via a discretized Boltzmann-equation. 2. Numerical results. J. Fluid Mech. 271, 311–339.
Ladd, A.J.C., Verberg, R., 2001. Lattice-Boltzmann simulations of particle–fluid suspensions. J. Stat. Phys. 104, 1191–1251.
Leboreiro, J., Joseph, G.G., Hrenya, C.M., Snider, D.M., Banerjee, S.S., Galvin, J.E., 2008. The influence of binary drag laws on MP-PIC simulations of segregating gas-fluidized beds. Powder Technol. 184, 275–290.
Lee, L., Leveque, R., 2003. An immersed interface method for incompressible Navier–Stokes equations. SIAM J. Sci. Comput. 25, 832–856.
Lucci, F., Ferrante, A., Elgobashi, S., 2010. Modulation of isotropic turbulence by particles of taylor length-scale size. J. Fluid Mech. 650.
Muldoon, F., Acharya, S., 2008. A divergence-free interpolation scheme for the immersed boundary method. Int. J. Numer. Methods Fluids 56, 1845–1884.
Nomura, T., Hughes, T.J.R., 1992. An arbitrary Lagrangian–Eulerian finite element method for interaction of fluid and a rigid body. Comput. Methods Appl. Mech. Eng. 95, 115–138.
Oguz, H., Prosperetti, A., 2001. Physalis: a new $o(n)$ method for the numerical simulation of disperse systems. J. Comput. Phys. 167, 196–216.
Pai, M.G., Subramaniam, S., 2009. A comprehensive probability density function formalism for multiphase flows. J. Fluid Mech. 628, 181–228.
Patankar, N., Singh, P., Joseph, D.D., Glowinski, R., Pan, T.W., 2000. A new formulation of the distributed Lagrange multipliers/fictitious domain method for particulate flow. Intl. J. Multiphase Flow 26, 1509–1524.
Patankar, S.V., 1980. Numerical Heat Transfer and Fluid Flow. Hemisphere Publ. Corp., McGraw-Hill.
Patil, D.J., Annaland, M.V., Kuipers, J.A.M., 2005. Critical comparisons of hydrodynamic models for gas–solid fluidized beds – Part I: Bubbling gas–solid fluidized beds operated with a jet. Chem. Eng. Sci. 60, 57–72.
Peskin, C.S., 1981. The fluid dynamics of heart valves: experimental, theoretical, and computational methods. Annu. Rev. Fluid Mech. 14, 235–259.
Pope, S.B., 2000. Turbulent Flows. Cambridge University Press, Port Chester, NY.
Richardson, J., Zaki, W.N., 1954. Sedimentation and fluidization: Part 1. Trans. Inst. Chem. Eng. 32, 35–53.
Sangani, A.S., Acrivos, A., 1982. Slow flow through a periodic array of spheres. Intl. J. Multiphase Flow 8, 342–360.
Scardovelli, R., Zaleski, S., 1999. Direct numerical simulation of free-surface and interfacial flow. Annu. Rev. Fluid Mech. 31, 567–603.
Schiller, L., Naumann, A., 1935. A Drag Coefficient Correlation. V.D.I. Zeitung.
Sharma, N., Patankar, N., 2005. A fast computation technique for the direct numerical simulation of rigid particulate flows. J. Comput. Phys. 205, 439–457.
Shen, L., Zheng, M., Xiao, J., Xiao, R., 2008. A mechanistic investigation of a calcium-based oxygen carrier for chemical looping combustion. Combust. Flame 154, 489–506.
Snyder, L.J., Stewart, W.E., 1966. Velocity and pressure profiles for Newtonian creeping flow in regular packed beds of spheres. AIChE J. 12, 167–173.
Sorensen, J.P., Stewart, W.E., 1974. Computation of forced-convection in slow flow through ducts and packed-beds. 2. Velocity profile in a simple cubic array of spheres. Chem. Eng. Sci. 29, 819–825.
Subramaniam, S., 2000. Statistical representation of a spray as a point process. Phys. Fluids 12, 2413–2431.
Sun, J., Battaglia, F., Subramaniam, S., 2007. Hybrid two-fluid dem simulation of gas–solid fluidized beds. J. Fluid Eng. 129, 1394–1403.
Syamlal, M., O'Brien, T.J., 1987. A generalized drag correlation for multiparticle systems. Tech. Rep., Morgantown Energy Technology Center DOE Report.
Syamlal, M., Rogers, W., O'Brien, T.J., 1993. MFIX documentation: theory guide. Tech. Rep. DOE/METC-95/1013, NTIS/DE95000031, National Energy Technology Laboratory, Department of Energy. <http://www.mfix.org>.
Takagi, S., Oguz, H., Zhang, Z., Prosperetti, A., 2005. Physalis: a new method for particle simulation. Part ii: Two-dimensional Navier–Stokes flow around cylinders. J. Comput. Phys. 187, 371–390.
Ten Cate, A., Derksen, J.J., Portela, L.M., van den Akker, H.E.A., 2004. Fully resolved simulations of colliding monodisperse spheres in forced isotropic turbulence. J. Fluid Mech. 519, 233–271.
Tenneti, S., Garg, R., Hrenya, C.M., Fox, R.O., Subramaniam, S., 2010. Direct numerical simulation of gas–solid suspensions at moderate Reynolds number: quantifying the coupling between hydrodynamic forces and particle velocity fluctuations. Powder Technol. 203, 57–69.
Uhlmann, M., 2005. An immersed boundary method with direct forcing for the simulation of particulate flows. J. Comput. Phys. 209, 448–476.
van der Hoef, M.A., Beetstra, R., Kuipers, J.A.M., 2005. Lattice-Boltzmann simulations of low-Reynolds-number flow past mono- and bidisperse arrays of sphere: results for the permeability and drag force. J. Fluid Mech. 528, 233–254.
Wen, C.Y., Yu, Y.H., 1966. Mechanics of fluidization. Chem. Eng. Prog. Symp. Ser. 62, 100–111.
Xu, S., Wang, Z., 2006. Systematic derivation of jump conditions for the immersed interface method in three-dimensional flow simulation. SIAM J. Sci. Comput. 27, 1948–1980.
Yi, C.K., Jo, S.H., Seo, Y., Lee, J.B., Ryu, C.K., 2007. Continuous operation of the potassium-based dry sorbent CO_2 capture process with two fluidized-bed reactors. Int. J. Greenhouse Gas Control 1, 31–36.
Yin, X., Sundaresan, S., 2009a. Drag law for bidisperse gas–solid suspensions containing equally sized spheres. Ind. Eng. Chem. Res. 48, 227–241.
Yin, X., Sundaresan, S., 2009b. Fluid–particle drag in low-Reynolds-number polydisperse gas–solid suspensions. AIChE J. 55, 1352–1368.
Yusof, J.M., 1996. Interaction of massive particles with turbulence. PhD thesis, Cornell University.
Zhang, D.Z., Prosperetti, A., 2003. A method for particle simulations. J. Appl. Mech. 70, 64–74.
Zhang, D.Z., Prosperetti, A., 2005. A second-order method for three-dimensional particle flow simulations. J. Comput. Phys. 210, 292–324.
Zick, A.A., Homsy, G.M., 1982. Stokes flow through periodic arrays of spheres. J. Fluid Mech. 115, 13–26.